NASA TECHNICAL NOTE
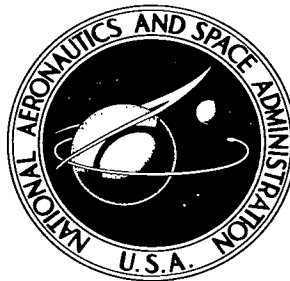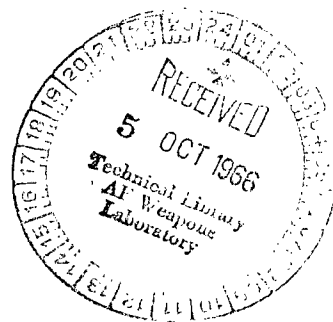
NASA TN D-3620

APOLLO AFTERBODY HEAT TRANSFER AND PRESSURE WITH AND WITHOUT ABLATION AT M_∞ OF 5.8 TO 8.3

by George Lee and Robert E. Sundell

Ames Research Center
Moffett Field, Calif.

NATIONAL AERONAUTICS AND SPACE ADMINISTRATION • WASHINGTON, D. C. • SEPTEMBER 1966

APOLLO AFTERBODY HEAT TRANSFER AND PRESSURE WITH AND

WITHOUT ABLATION AT M_∞ OF 5.8 TO 8.3

By George Lee and Robert E. Sundell

Ames Research Center
Moffett Field, Calif.

APOLLO AFTERBODY HEAT TRANSFER AND PRESSURE WITH AND

WITHOUT ABLATION AT M_∞ OF 5.8 TO 8.3

By George Lee and Robert E. Sundell
Ames Research Center

SUMMARY

Apollo afterbody pressures and heat transfer with and without an ablating nose cap have been measured at Mach numbers 5.8 to 8.3, stream enthalpies of 1.628×10^6 to 9.296×10^6 J/kg, and Reynolds numbers based on diameter of 200 to 22,000. Correlations of the data and comparisons with theories have been made.

INTRODUCTION

Ablation type heat shields, commonly used for the thermal protection of the stagnation region of spacecraft, inject gases into the stream. The question of how ablation products affect the downstream portion of the spacecraft has been considered for simple shapes, such as flat plates, wedges, cones, and hemisphere cylinders (refs. 1 to 10), and the results indicate that the upstream injection of gases can significantly change pressures and heat transfer. For more complicated shapes very little information is available about effects of injection of ablation products. For a configuration like the Apollo, the situation is further complicated by the fact that the downstream flow can be either attached or separated. Since heat transfer and pressures are quite different for attached and separated flows, the influence of ablated gases is also likely to be different.

In this report, an experimental investigation of the heat transfer and pressures to the afterbody of an Apollo model with an ablating Teflon nose cap is presented and compared with approximate theories developed herein. The experiments were conducted at Mach numbers from 5.8 to 8.2, stream enthalpies from 1.628×10^6 to 9.296×10^6 J/kg, and Reynolds numbers based on model diameter from 200 to 22,000.

SYMBOLS

C constant of proportionality in viscosity-temperature relation

C_D drag coefficient

c_p specific heat of air, J/kg-$^\circ$K

c_{p_m} specific heat of metal, J/kg-$^{\mathrm{O}}$K

D model diameter, m

D_n drag force, N

$f(\eta)$ Blasius dimensionless stream function

h total enthalpy, J/kg

H_{eff} effective heat of ablation, J/kg

I, J, K shear layer integrals used in separated flow theory and defined in reference 6

$\left.\begin{array}{l} I_1r(\eta), \\ I_1s(\eta) \end{array}\right\}$ integral of the temperature functions

k thermal conductivity, J/m-sec-$^{\mathrm{O}}$K

t wall thickness, m

L reference length, m

$\dot{m}$ mass injection rate, kg/m^2-sec

M Mach number

p pressure, N/m^2

$\bar{p}$ average pressure, N/m^2

Δp difference in pressure, $p_a - p_{na}$, N/m^2

Pr Prandtl number, $\mu c_p / k$

$\dot{q}$ heat-transfer rate, J/m^{2}sec

$\bar{\dot{q}}$ average heat-transfer rate, J/m^{2}sec

$\Delta\dot{q}$ difference in heat-transfer rate, $\dot{q}_a - \dot{q}_{na}$, J/m^{2}sec

Q integrated heat-transfer rate, J/sec

Q^* dimensionless heat-transfer parameter defined in equation (A3)

R maximum cross-sectional radius of model, m

$\mathcal{R}$ gas constant

Re Reynolds number, $\rho u x / \mu$

2

Re_L — Reynolds number, $\rho_\infty u_\infty L / \mu_\infty$

r — temperature function (eq. (B13))

r_c — corner radius of model, m

r_n — nose radius of model, m

S — model surface distance measured from stagnation point, m

$s*$ — dimensionless compressible streamwise distance function (eq. (A1))

s — temperature function (eq. (B14))

St — Stanton number, $\dot{q}/\rho_\infty u_\infty (h_t - h_w)$

T — temperature, deg

u, v — velocity components parallel to the x and y axes, respectively

U — velocity, m/sec

u_s — velocity at edge of boundary layer

$u*$ — dimensionless velocity used in separated flow theory and defined in reference 6

$\dot{v}$ — stagnation-point recession rate, m/sec

x, y — rectangular coordinates in directions parallel and normal, respectively, to the free-stream velocity with origin at the nose

$\left.\begin{array}{c} Y_b \\ Y_e \\ Y_w \end{array}\right\}$ — the y ordinates of the inner edge of the entropy layer, the outer edge of the entropy layer, and the body surface, respectively

Z — variable related to Y_e (eq. (B22))

α — angle of attack, deg

α_1 — asymptotic value appearing in equation (B20)

γ — specific heat ratio

$\delta*$ — boundary-layer displacement thickness, m

ϵ — $\gamma-1/\gamma+1$

ζ — variable related to x in equation (B23)

ξ, η — two spatial variables used in boundary analysis (eq. (B5))

3

κ_ϵ parameter controlling inviscid tip bluntness effect (eq. (B21))

Θ $(h - h_W)/(h_\infty - h_W)$

λ, φ variables defined in equation (B25a)

μ coefficient of viscosity, kg/m-sec

ν wake angle, deg

ρ density, kg/m³

τ time, sec

Φ function whose derivative $\partial \Phi / \partial \eta$ is u/u_∞

χ_{ϵ_i} parameter governing the boundary-layer displacement effect (eq. (B20))

Ω_D, Ω_C dimensionless total enthalpy used in separated flow analysis

Subscripts

a   ablation

av   average

b   separation point on body

e   edge of boundary layer

na   no ablation

s   stagnation condition

t   reservoir condition

w   wall condition

∞   free-stream conditions

CONVERSION FACTORS

Item	Metric units	English units	Conversion factor - metric to English
Length	meter, m	feet, ft	3.281
Mass	kilogram, kg	lb_m	2.206
Force	newton, N	lb_f	.2248
Energy	joules, J	Btu	.9488 (10^{-3})
Density	kg/m^3	lb_m/ft^3	.06250
Mass flux	kg/m^2-sec	lb_m/ft^2-sec	.2048
Pressure	N/m^2	$lb_f/in.^2$	.1451 (10^{-3})
Viscosity	kg/m-sec	lb_m/ft-sec	.6724
Specific heat	J/kg-^{O}K	Btu/lb_m-^{O}R	.2388 (10^{-3})
Enthalpy	J/kg	Btu/lb_m	.4303 (10^{-3})
Thermal conductivity	J/m-sec-^{O}K	Btu/ft-sec-^{O}R	.1606 (10^{-3})
Heat-transfer rate	J/m^2-sec	Btu/ft^2-sec	.8814 (10^{-4})
Integrated heat-transfer rate	J/sec	Btu/sec	.9488 (10^{-3})

Multiply metric units by conversion factor to obtain English units.

APPARATUS

Test Facility

The tests were conducted in a hypersonic free-jet wind tunnel at Ames Research Center. The facility is described in reference 11. The air stream was heated by a rotating-type electric arc heater; the total stream enthalpy was varied between 1.628×10^6 and 9.296×10^6 J/kg; and the stagnation pressures were varied between 2.5 and 10 atm. Nominal Mach numbers were varied between 5.8 and 8.3. Typical Mach number surveys are presented in figure 1. The test conditions are listed in table I.

Models

The model configuration was a 0.0065-scale model of the Apollo command module. The geometric details of the model are shown in figure 2.

The heat-transfer model was made in two parts: a nose cap and a thin-shelled stainless-steel afterbody. The shell was 3.81×10^{-5} m thick. The nose

cap of the ablating model was Teflon and that of the nonablating model was steel. A single thermocouple was located at the midpoint of the afterbody.

The ablating and nonablating pressure models were made entirely of Teflon and steel, respectively. An orifice of 8.1×10^{-4} m diameter was located at the midpoint of the afterbody.

Support System

The model was supported from the rear by a hollow sting which served as a conduit for the thermocouple and pressure leads.

For the heat-transfer test with ablating models a thin-shell half-conical shield made of steel and lined with asbestos was used to shield the afterbody of the model until the Teflon nose cap reached steady-state ablation.

Instrumentation

Model temperatures were measured with chromel-alumel thermocouples spot-welded to thermally insulated steel-slug calorimeters. Thermocouple voltages were recorded on an oscillograph.

Model pressures were measured with vibrating-diaphram pressure cells described in reference 12. Voltage output from the cells was read on a digital voltmeter and also recorded on an oscillograph.

Test Technique and Data Reduction

Heat-transfer measurements were made by the thin-skin, transient-heating technique. The models were initially at ambient temperature. The afterbody of the nonablating model was exposed to the stream by removing a shield when the tunnel flow was established. The afterbody of the ablating model was exposed to the stream by removing a shield when the Teflon nose cap reached 90 percent of the steady-state ablation rate as calculated by the method of reference 13. The skin temperature increased linearly with time for approximately the first 4 seconds of the test. The heating rates were computed from the temperature time history by the following equation:

$$\dot{q} = \rho_w c_{p_m} t \, dT_w/d\tau$$

No corrections were made to the heat transfer for conduction effects. It is believed that the conduction effects were small because of the thinness of the wall and relatively low conductivity of the steel.

Pressure measurements were made by observing the pressure cell output voltage on a digital voltmeter. Measurements were taken when the voltage (i.e., pressure) was steady with time. The time to reach steady pressures on

the steel model was a few seconds, but on the ablating model it corresponded roughly to the time required by the Teflon nose cap to reach steady-state ablation.

The mass injection rate for $\alpha = 0°$ was calculated by the following equation

$$\dot{m} = (\rho\dot{v})_{Teflon} \tag{1}$$

where the stagnation-point recession rate, $\dot{v}$, was calculated by the stagnation-point ablation analysis of reference 13. This analysis should give a good approximation because the heating rate over the nose cap was essentially constant. The calculated recession rates as a function of time for four typical test conditions are shown in figure 3.

The steady-state recession rate, used in correlating the experimental data at $\alpha = 0°$, was taken as 90 percent of the theoretical asymptotic value. An experimental steady-state recession rate was not used because of the large number of data points required. The 90-percent value was chosen because the experimental afterbody pressures were usually steady at the run time corresponding to the 90-percent value. This indicated that although steady-state recession theoretically was not attained, the effect on the measured afterbody pressures was small.

To confirm the accuracy of the method of reference 13, a comparison of the measured and calculated stagnation-point recession distance is presented in figure 4. As can be seen, the agreement between the measured and the calculated values is excellent.

The mass injection rates for the $\alpha = 33°$ cases were found by the following semiempirical formula of reference 14:

$$\dot{m} = \bar{q}/H_{eff}$$

where for Teflon, $H_{eff} = 950 + 0.44 (h_t - h_w)$. In this case, $\bar{q}$ is the average heating rate over either the windward or leeward side of the nose cap. The average heating rate was obtained from measured heating-rate distributions for no mass injection.

RESULTS AND DISCUSSION

The basic heat-transfer and pressure data for the ablating Teflon and nonablating steel models are presented in figures 5 and 6, respectively. The data in these figures are plotted against the nominal test conditions listed in table I. (Note that for heat-transfer tests, test condition I is absent.) To determine the effects of mass injection on the afterbody heat transfer and pressure, comparisons should be made for a given test condition only and not between different test conditions because of the differences in Mach number and Reynolds number. Except for the heat-transfer rates on the windward side

of the model at $\alpha = 33^O$ which showed no effect of mass injection, heat-transfer rates were lowered (by as much as 1/2) and the pressures were increased (by as much as 1/4) by the mass injection. The lowering of the heating rates at $\alpha = 0^O$ agrees with the results of a free-flight experiment (see ref. 15) which showed that mass injection from an ablating nylon nose cap lowered the afterbody heating by nearly 1/2.

Since the heat transfer and pressure were affected by the mass injection rate, Mach number, and Reynolds number, correlation parameters which consider all these variables will be required when data are compared for different test conditions. A brief description of the theories from which such parameters were obtained will be given next and correlations of the data in terms of these parameters will follow.

Separated Flow

The separated flow theory of Baum, King, and Denison (refs. 6-9) was used to obtain a correlation parameter for the $\alpha = 0^O$ and 33° leeward flow. This theory was an extension of Chapman's theory for laminar separated flow (ref. 16) to include a finite boundary layer at the separation point and mass injection from the body surface.

Before the correlation parameter obtained from the theory is presented the validity of the theory for the $\alpha = 0^O$ flow and the $\alpha = 33^O$ leeward side flow will be discussed briefly. It must be shown that the following assumptions are satisfied:

1. Flow is separated over the afterbody surfaces at $\alpha = 0^O$ and $\alpha = 33^O$ on the leeward side.

2. Injected gas and free-stream gas are the same.

3. The distribution of injected gas is proportional to $\sqrt{x}$.

Discussion of Assumptions

1. Evidence that the flow was separated over the afterbody at $\alpha = 0^O$ and over the leeward side at $\alpha = 33^O$ can be seen in the oil-film pictures of figure 7. The separated flow regions are indicated by little or no disturbance of the oil film because shear forces are low; whereas, the attached flow regions ($\alpha = 33^O$ windward side) flow lines are established by the higher shear forces.

2. Assumption 2 was not accurate since the injected gas was Teflon and the free-stream gas was air. The effect of such a difference on the afterbody pressure and heat transfer is indicated by reference 17; injecting a heavy gas, like Teflon vapor, increases heat transfer more than injecting a lighter gas, such as air.

3. As shown in figure 8, the experimental injected mass distribution over the nose cap was not proportional to $\sqrt{x}$ for $\alpha = 0°$. For $\alpha = 33°$, this assumption was more closely matched. The effect of not meeting this assumption cannot be assessed.

Now that the validity of the assumptions has been discussed, a correlation parameter (i.e., the modified stream function) $f(0)$ will be presented from the theory. From appendix A, where the pertinent equations of the theory are given, $f(0)$ for $\alpha = 0°$ and $33°$ was found to be

$$f(0) = -0.75 \sqrt{Re_L} \left[\frac{(\dot{m})_{Teflon}}{(\rho_e \mu_e)_{av}} \right] \quad \text{for} \quad \alpha = 0° \quad (A7)$$

$$f(0) = -1.2 \sqrt{Re_L} \left[\frac{(\dot{m})_{Teflon}}{(\rho_e \mu_e)_{av}} \right] \quad \text{for} \quad \alpha = 33° \text{ leeward side} \quad (A8)$$

It is noted that the parameter $f(0)$ is an incomplete correlation parameter in the sense that it does not explicitly contain all the variables of the problem. However, it does contain two of the major ones, namely, the Reynolds number and the mass injection rate ratio.

The experimental heat transfer and pressure are plotted in figure 9 along with the predictions of Baum, King, and Denison. The experimental data correlate fairly well on $f(0)$. The data trends are predicted by the theory but the agreement of absolute magnitudes is not very good over the complete range of $f(0)$.

As seen in figure 9, the effect of mass injection, experimentally and theoretically, was to raise the pressure and to lower the heat transfer. The increased pressure was caused by a lower "dividing-streamline velocity" as a result of mass injection. According to the "recompression condition" of Chapman (ref. 16), this lengthens the wake and lessens the expansion at the separation point, resulting in a higher pressure. The lower heat transfer was due to the injected gases of lower temperature being entrained by the separated flow.

Attached Flow

For attached flow at $\alpha = 33°$, correlation parameters were developed in appendix B by extending H. K. Cheng's blunt-nosed flat-plate viscous interaction theory (refs. 18 and 19) to include surface mass injection. The choice of a blunt-nosed flat plate to represent the attached flow over the model at $\alpha = 33°$ was based on the results of reference 20 which showed that the pressure distribution on the windward side of an Apollo model can be represented quite well by two-dimensional blast-wave theory.

Before presenting the correlation parameters obtained from the theory, a brief discussion of the following assumptions of the theory and how well each of these assumptions was met in the experimental case will be given.

1. Injected gas is the same as free-stream gas.

2. Distribution of injected mass is proportional to $x^{-5/6}$.

3. The disturbance velocity $(u/u_\infty - 1)$ as well as the square of the flow angle in the inviscid flow field must be negligibly small in comparison to unity.

4. The specific heat ratio must be sufficiently close to unity.

5. The bow shock must be sufficiently strong.

6. Vorticity interaction effects are small and the Blasius boundary-layer solution is used between the shear layer and the body surface.

Discussion of Assumptions

1. The same comments apply as in assumption 2 of the separated flow theory.

2. The $x^{-5/6}$ variation in mass distribution was not met for the heat-transfer tests, but was for the pressure tests. (See fig. 10.) Because of the differences in model construction, the ablation on the heat transfer model stopped at a distance of 3 corner radii downstream of the nose; whereas, there was ablation further downstream on the pressure model. According to reference 3 the heat transfer should be higher for discontinuous injection than for the continuous injection.

3. The small disturbance velocity and flow angle were satisfied except in the region near the nose.

4. Assumption 4, that γ be close to unity, was not met. This, however, was not important since the assumption of $\gamma = 1$ permitted the dropping of the pressure gradient term in the momentum equation and this same result is also achieved by a "cold wall" boundary layer (cf. L. Lees, ref. 21).

5. The strong shock assumption was satisfied.

6. According to Cheng, errors from vorticity interaction will probably be no larger than those incurred by the approximation of small disturbance velocity (i.e., assumption 5).

The correlation parameters were obtained from the following equations developed in appendix B for the pressure and heat transfer on the flat plate.

$$\frac{p}{p_\infty} \frac{1}{4\gamma_\infty} \left(\frac{\kappa\epsilon}{x^2 \epsilon_i}\right)^2 = G(\lambda) \tag{B30}$$

$$-\text{St}\ \frac{\text{Pr}M_\infty}{2s'(0)\sqrt{\gamma_\infty}}\left[\alpha_1 + \frac{\gamma_\infty-1}{2}M_\infty^2 I_1 r(\infty) + \left(\frac{T_w}{T_\infty} - \frac{T_{aw}}{T_\infty}\right)I_1 s(\infty)\right]\left(\frac{\kappa_\epsilon}{\chi_{\epsilon_i}^2}\right)^3 = \frac{G(\lambda)}{\sqrt{\displaystyle\int_0^\lambda G(\lambda)\zeta'\ d\lambda}}$$

$$(B31)$$

    With the solutions in this form, it is natural to choose the left side of
equations (B30) and (B31) as the ordinate of the correlation plots for
pressures and heat transfer, respectively. The right-hand side of the equa-
tions can be related to $\chi_{\epsilon_i}/\kappa_\epsilon^{2/3}$ (see eqs. (B23) and (B28)). Hence
$\chi_{\epsilon_i}/\kappa_\epsilon^{2/3}$ was chosen as the abscissa of both the pressure and heat-transfer
correlation plots because, for a given set of test conditions, $\chi_{\epsilon_i}/\kappa_\epsilon^{2/3}$ is
proportional to $x^{1/6}$. The bracketed term in the parameter

$$\chi_{\epsilon_i} = 2M_\infty\sqrt{\frac{C}{\text{Re}_L}}\left[\alpha_1 + \frac{\gamma-1}{2}M_\infty^2 I_1 r(\infty) + \left(\frac{T_w}{T_\infty} - \frac{T_{aw}}{T_\infty}\right)I_1 s(\infty)\right]$$

(see eq. (20)) is a function of the injection rate since α_1, $I_1 r(\infty)$, $I_1 s(\infty)$
are functions of $f(0)$. Increasing the injection rate or the wall temperature
will increase χ_{ϵ_i}. The term $\kappa_\epsilon = 2\epsilon M_\infty^3 C_D \dfrac{r_c}{x}$ is independent of the
injection rate and is a function of the inviscid flow and model geometry.

    The attached flow heat-transfer and pressure data are plotted versus the
parameters shown in equations (B31) and (B30) in figures 11(a) and 11(b),
respectively. There are four distinct groups of data which varied over three
orders of magnitude in the parameters shown on the ordinate. The large varia-
tion is caused by the changing Mach number and Reynolds number. Therefore the
plot is primarily a correlation of the effects of Mach and Reynolds numbers.
Although the effects of mass injection are also included in this plot through
the parameter χ_{ϵ_i}, the effects of the mass injection cannot be readily seen
in this plot for the following reasons: (1) χ_{ϵ_i} is a complicated function of
the mass injection rate, (2) χ_{ϵ_i} appears in the abscissa and ordinate (raised
to the 1/4 and 1/5 power for the pressure and heat transfer, respectively),
and (3) the effect of mass injection for the present tests is less than 40 per-
cent and therefore is not readily seen on a logarithmic plot. The data will
be plotted in terms of the mass injection parameter later.

    Comparisons of the heat-transfer and pressure data with theory are also
presented in figures 11(a) and 11(b). The agreement between theory and the
data (due primarily to Mach and Reynolds number effects) is only fair.
Differences as large as a factor of 2 are present. These differences can be
attributed to the fact that many of the assumptions of the theory were not
satisfied experimentally. For the same reasons stated previously, a comparison
of the theoretical and experimental effects of mass injection cannot be readily
made from this figure.

The heat-transfer and pressure data plotted against the mass injection parameter $f(0)$ (at constant M_∞ and Re_L) are presented in figures 12(a) and 12(b), respectively. Experimentally and theoretically, the effect of mass injection was to raise the pressure. The increased pressure was probably due to a larger displacement thickness as a result of the injected gases. The effect of mass injection was to lower the heat transfer theoretically, but not experimentally. The probable reason why the mass injection did not affect the heat transfer in the experimental case was that the mass injection occurred on the nose tip only. According to reference 3, the heat transfer for this type of discontinuous injection quickly approaches that for no injection a short distance downstream of the point of injection.

CONCLUSIONS

From the results of the experiment and theory for the model at $\alpha = 0^\circ$ and 33°, the following conclusions were reached:

1. Ablation increased the afterbody pressures in the separated and attached flow regions.

2. Ablation decreased the afterbody heat transfer in the separated flow regions, but had a negligible effect in the attached flow region.

3. For separated flows, heat transfer and pressure were correlated in terms of the modified stream function. For attached flows, the data were correlated in terms of the inviscid tip bluntness and boundary-layer displacement parameters.

Ames Research Center
National Aeronautics and Space Administration
Moffett Field, Calif., June 3, 1966
129-03-12-01

APPENDIX A

CALCULATION PROCEDURE FOR SEPARATED FLOWS

An outline of the method of calculation and the pertinent equations are given below. The charts required for the calculations were taken from reference 6. A sketch of the separated flow region is given in figure 13(a).

The method for calculating pressures involved an iterative procedure in which the pressure ratio p_4/p_3 (i.e., pressure downstream of the recompression shock to the pressure in the separated region) was calculated by inviscid and viscous flow analyses and compared with each other. When p_4/p_3 ratios are matched, the problem is considered solved.

1. For the inviscid or outer flow problem, assume a value of ν, the expansion angle of the wake. With this angle, p_4/p_3 was found by two-dimensional wedge flow methods.

2. For the viscous or inner flow problem, p_4/p_3 was found as follows:

    (a) Take the ν from the inviscid case.

    (b) Compute $s*$ as follows:

$$s* = \frac{s}{s_b} = \frac{\int_{s_b}^{s_o} C_3 \rho_3 u_3 \mu_3 r \, ds}{\int_{0}^{s_b} C_2 \rho_2 u_2 \mu_2 r \, ds (\rho_e u_e \mu_e)_2} = k_1 \left(\frac{p_3}{p_s}\right)^{0.9} \sqrt{1 - \left(\frac{p_3}{p_s}\right)^{1/6}} \frac{1}{\sin \beta} \tag{A1}$$

where for the nominal test conditions

$$k_1 = 5.5 \quad \text{for} \quad \alpha = 0^\circ$$

$$k_1 = 12.5 \quad \text{for} \quad \alpha = 33^\circ \text{ leeward side}$$

3. $u*$ can be found from a plot of $u*$ vs. $s*$ (fig. 6 of ref. 6).

4. Solve for Ω_C and Ω_D as follows:

$$\Omega_C = \frac{K - J + Q*}{I - J}$$

$$\Omega_D = W_D(1 - \Omega_C) + \Omega_C(1 - u*)$$

where I, J, K, W_D are taken from plots in reference 6 and

$$Q^* = \frac{Q}{2\pi(h_s - h_w)\sqrt{S_b}} = 0.32\sqrt{\left(\frac{p_3}{p_s}\right)^{0.9}\left[1 - \left(\frac{p_3}{p_s}\right)^{1/6}\right]^{1/2}}$$

5. p_4/p_3 from the viscous solution can now be solved as follows:

$$\frac{p_4}{p_3} = \left[1 + \frac{\frac{\gamma-1}{2}u^{*2}M_3{}^2}{1 + \frac{\gamma-1}{2}M_3{}^2(1 - u^{*2}) - \left(1 + \frac{\gamma-1}{2}M_3{}^2\right)\left(1 - \frac{h_w}{h_s}\right)\Omega_D}\right]^{\frac{\gamma}{\gamma-1}}$$

(A2)

The equation for the afterbody heat transfer was taken from reference 7; namely,

$$Q^* = K(Q/Q_W)$$

(A3)

From this, the ratio of the total base heat-transfer rate with and without injection is

$$\frac{Q_a}{Q_{na}} = \frac{K_{na}Q_a^*}{K_a Q_{na}^*}$$

(A4)

CORRELATION PARAMETER

The modified stream function f(0) chosen to correlate the data was obtained by equating the integrated Teflon mass injection rate obtained by the theory of reference 13 or 14 to the theoretical flat-plate mass distribution of reference 22. The resulting equation is

$$\left(\frac{\dot{m}_{Teflon}}{\rho_e u_e}\right) \times L = \int_0^L \left(\frac{\rho_w v_w}{\rho_e u_e}\right)_{theory} dx$$

(A5)

The theoretical mass distribution is

$$\left(\frac{\rho_w v_w}{\rho_e u_e}\right)_{theory} = -\frac{1}{2}\sqrt{\frac{C}{Re_x}}\,f(0)$$

(A6)

where ρ_e, u_e are average edge conditions over the nose.

14

Therefore, by integrating equation (A5),

at $\alpha = 0°$

$$f(0) = -0.75 \sqrt{Re_L} \left[\frac{\dot{m}_{Teflon}}{(\rho_e u_e)_{av}}\right] \tag{A7}$$

at $\alpha = 33°$

$$f(0) = -1.2 \sqrt{Re_L} \left[\frac{\dot{m}_{Teflon}}{(\rho_e u_e)_{av}}\right] \tag{A8}$$

15

APPENDIX B

THEORY FOR ATTACHED FLOW

The theory used for the attached flow case ($\alpha = 33^O$ windward side) was an extension of H. K. Cheng's theory (refs. 18 and 19) for hypersonic viscous flow over a blunt-nosed flat plate to include the effect of mass injection. The development of the extended theory is presented below. Only the equations required to show the effects of injection are developed. All other equations are taken from reference 18. A sketch of the flow field around the plate is shown in figure 13(b).

GOVERNING EQUATIONS

The steady laminar flow of a viscous compressible fluid in a boundary layer on a blunt-nosed flat plate is governed by the momentum equation

$$u \frac{\partial u}{\partial x} + v \frac{\partial u}{\partial y} = \frac{1}{\rho} \frac{\partial}{\partial y} \left(\mu \frac{\partial u}{\partial y} \right) - \frac{1}{\rho} \frac{\partial p}{\partial x} \tag{B1}$$

the equation of continuity

$$\frac{\partial(\rho u)}{\partial x} + \frac{\partial(\rho v)}{\partial y} = 0 \tag{B2}$$

the energy equation

$$\rho c_p \left(u \frac{\partial T}{\partial x} + v \frac{\partial T}{\partial y} \right) = \frac{\partial}{\partial y} \left(k \frac{\partial T}{\partial y} \right) + \mu \left(\frac{\partial u}{\partial y} \right)^2 + u \frac{\partial p}{\partial x} \tag{B3}$$

and the equation of state

$$p = \rho R T \tag{B4}$$

these equations are subject to the following conditions:

$$\left. \begin{array}{l} v = 0 \\ v = v(x) \\ T = T_w \end{array} \right\} \text{ at } y = 0 \quad \text{and} \quad \left. \begin{array}{l} u = u_\infty \\ T = T_\infty \end{array} \right\} \text{ at } y = \infty$$

The variables x, y in the boundary-layer equations are now transformed as follows:

$$\xi = \int_0^x C \frac{p}{p_\infty} \frac{dx}{L} \tag{B5a}$$

$$\eta = \frac{\sqrt{Re_L} \int_0^y \frac{\rho}{\rho_\infty} \frac{dy}{L}}{\sqrt{\int_0^x C \frac{p}{p_\infty} \frac{dx}{L}}} \tag{B5b}$$

Assuming a linear viscosity-temperature relation

$$\frac{\mu}{\mu_\infty} = C \frac{T}{T_\infty}$$

and a constant Prandtl number of 0.72, the system of differential equations governing the boundary-layer problem is reduced to

$$2 \frac{\partial^3 \Phi}{\partial \eta^3} + \Phi \frac{\partial^2 \Phi}{\partial \eta^2} - 2\xi \left(\frac{\partial \Phi}{\partial \eta} \frac{\partial^2 \Phi}{\partial \xi \, \partial \eta} - \frac{\partial \Phi}{\partial \xi} \frac{\partial^2 \Phi}{\partial \eta^2} \right)$$

$$= \epsilon \left(\frac{2}{p^2} \frac{\partial p}{\partial x} \int_0^x p \, dx \right) \left[\frac{T_w}{T_t} + \left(1 - \frac{T_w}{T_t} \right) \Theta - \left(\frac{\partial \Phi}{\partial \eta} \right)^2 \right] \tag{B6a}$$

$$2 \frac{\partial^2 T}{\partial \eta^2} + Pr \Phi \frac{\partial T}{\partial \eta} + 2Pr\xi \left(\frac{\partial \Phi}{\partial \xi} \frac{\partial T}{\partial \eta} - \frac{\partial \Phi}{\partial \eta} \frac{\partial T}{\partial \xi} \right)$$

$$= -2Pr(\gamma - 1)M_\infty^2 T_\infty \left(\frac{\partial^2 \Phi}{\partial \eta^2} \right)^2 - \frac{2}{\rho} \frac{Pr}{c_p} \frac{p_\infty}{p} \frac{\partial \Phi}{\partial \eta} \frac{\partial p}{\partial x} \int_0^x p \, dx \tag{B6b}$$

and the boundary conditions

$$\left. \begin{array}{lll} \dfrac{\partial \Phi}{\partial \eta} = 0 & \text{at} \quad \eta = 0 \\[2ex] \Phi = 0 & \text{at} \quad \eta = 0 \text{ for no injection} \\[2ex] \Phi = \text{const} & \text{at} \quad \eta = 0 \text{ with injection} \end{array} \right\} \tag{B6c}$$

where

$$\frac{u}{u_\infty} = \frac{\partial \Phi}{\partial \eta}$$

The normal or mass injection velocity at the wall can be found by integrating the continuity equation to obtain

$$v_w = -\frac{1}{2}\frac{p}{p_\infty}\frac{\rho_\infty}{\rho_w}\frac{u_\infty}{\sqrt{Re_L}}\frac{\sqrt{C}}{\sqrt{\int_o^x \frac{p}{p_\infty}\frac{dx}{L}}}\left[\Phi(\xi,0) + 2\xi\Phi(\xi,0)\right] \tag{B7a}$$

The leading approximation of v_w is

$$v_w = -\frac{1}{2}\frac{p}{p_\infty}\frac{\rho_\infty}{\rho_w}\frac{u_\infty}{\sqrt{Re_L}}\frac{\sqrt{C}}{\sqrt{\int_o^x \frac{p}{p_\infty}\frac{dx}{L}}}\left[f(0)\right]$$

The modified stream function, $f(0)$, which determines the effect of injection on heat transfer and pressure, is solved from equation (B7a) by equating the integrated Teflon mass rate (ref. 14) to the integrated theoretical mass rate as follows:

$$\left(\frac{\dot{m}}{\rho_\infty u_\infty}\right)_{Teflon} L_1 = \int_o^{L_2}\frac{\rho_w v_w}{\rho_\infty u_\infty}dx = -\frac{f(0)}{2}\sqrt{\frac{C}{Re_L}}\int_o^{L_2}\frac{p/p_\infty}{\sqrt{\int_o^{L_2}(p/p_\infty)(dx/L)}} \tag{B7b}$$

L_1 is the length on the experimental model which is ablating and L_2 is the total length of the model. For the heat-transfer model, L_1 was less than L_2 because ablation stopped slightly downstream of the nose. For the pressure model, $L_1 = L_2$ because ablation occurred along the entire length of the model. Before equation (B7b) can be solved, the pressures over the plate must be known. To the first approximation, the asymptotic solution of reference 18 for the pressures near the nose of the plate

$$\frac{p}{p_\infty} = \left(\frac{1}{18}\right)^{1/3}\kappa_\epsilon^{2/3}$$

shall be used. The modified stream function was found to be

$$f(0) = 0.13(Re_D)^{1/2}\left(\frac{\dot{m}}{\rho_\infty u_\infty}\right)_{Teflon}\frac{r_c x^{1/6}}{M_\infty} \tag{B7c}$$

The leading approximation to the solution of the system of equations (B6) for $\epsilon \to 0$ according to Cheng is

$$2\frac{d^3\Phi}{d\eta^3} + \Phi\frac{d^2\Phi}{d\eta^2} = 0 \tag{B8}$$

or in the more familiar notation

18

$$f''' + ff'' = 0 \qquad\qquad (B9)$$

where $f' = 2u/u_\infty$ and

$$T'' + PrfT' = -\frac{\gamma-1}{4} M_\infty{}^2 T_\infty Pr(f'')^2 \qquad\qquad (B10)$$

where the primes denote total derivatives with respect to η.

The momentum equation thus becomes the Blasius equation with a nonvanishing initial value. Solutions of the problem can be found in reference 23.

The energy equation[1] can be solved by methods described by Chapman and Rubesin (ref. 24). Some numerical solutions of this equation can be found in reference 22. Following the method of reference 22, the energy equation can be split into two linearly related parts:

$$\frac{T}{T_\infty} = 1 + \frac{\gamma-1}{2} M_\infty{}^2 r(\eta) + \left(\frac{T_w}{T_\infty} - \frac{T_{aw}}{T_\infty}\right) s(\eta) \qquad\qquad (B11)$$

T_{aw} is the adiabatic wall temperature given by

$$\frac{T_{aw}}{T_\infty} = 1 + \frac{\gamma-1}{2} M_\infty{}^2 r(0) \qquad\qquad (B12)$$

and r and s satisfy

$$\left. \begin{aligned} & r'' + Prfr' = -\frac{Pr}{2} (f'')^2 \\ & r'(0) = 0, \qquad r(\infty) = 0 \end{aligned} \right\} \qquad\qquad (B13)$$

$$\left. \begin{aligned} & s'' + Prfs' = 0 \\ & s(0) = 1, \qquad s(\infty) = 0 \end{aligned} \right\} \qquad\qquad (B14)$$

The surface heat transfer and the boundary-layer displacement thickness are found to be

$$St = \frac{\dot{q}}{\rho_\infty u_\infty (h_{aw} - h_w)} = \frac{-k \left.\frac{\partial T}{\partial y}\right)_w}{\rho_\infty u_\infty (h_{aw} - h_w)} = -\frac{s'(0)}{2Pr} \sqrt{\frac{C}{Re_L}} \frac{\dfrac{p}{p_\infty}}{\sqrt{\displaystyle\int_0^x \frac{p}{p_\infty} \frac{dx}{L}}}$$

$$(B15)$$

$$\frac{\delta^*}{L} = 2\left[\alpha_1 + \frac{\gamma-1}{2} M_\infty{}^2 Ir(\infty) + \left(\frac{T_w}{T_\infty} - \frac{T_{aw}}{T_\infty}\right) Is(\infty)\right] \frac{p}{p_\infty} \sqrt{\frac{C}{Re_L}} \int_0^x \frac{p}{p_\infty} \frac{dx}{L}$$

$$(B16)$$

---

[1]Note that equation (B10) is not the simplified energy equation of Cheng's.

From Cheng's analysis of the conservation of mass and entropy in the entropy layer (i.e., the layer bounded by the shock wave and the outer edge of the boundary layer) a pressure-area relation in the entropy region assuming $\gamma = 1$ was developed, namely,

$$(Y_e - Y_b)p = \frac{\epsilon D_n}{\rho_\infty U_\infty^2} \tag{B17}$$

The pressure can be approximated by the Newtonian-plus centrifugal formula

$$p \simeq \rho_\infty U_\infty^2 (Y_e Y_e')'$$

Therefore equations (B17) and (B16) can be written

$$(Y_e - Y_w - \delta^*)(Y_e Y_e')' = \epsilon C_D r_c \tag{B18}$$

$$\delta^* = \frac{\sqrt{x}}{M_\infty^2} \chi_{\epsilon_i} \frac{\sqrt{Y_e Y_e'}}{(Y_e Y_e')'} \tag{B19}$$

These are the equations governing the zero-order approximation of the problem; χ_{ϵ_i} is defined as follows:

$$\chi_{\epsilon_i} = \frac{2M_\infty \sqrt{C}}{\sqrt{Re_L}} \left[\alpha_1 + \frac{\gamma-1}{2} M_\infty^2 I_1 r(\infty) + \left(\frac{T_w}{T_\infty} - \frac{T_{aw}}{T_\infty} \right) I_1 s(\infty) \right] \tag{B20}$$

By introducing the following new variables

$$\kappa_\epsilon = 2M_\infty^3 \epsilon C_D \frac{r_c}{x} \tag{B21}$$

$$Z = 8M_\infty \left(\frac{\chi_{\epsilon_i}^2}{\kappa_\epsilon} \right)^2 \frac{Y_e}{\kappa_\epsilon x} \tag{B22}$$

$$\zeta = 16 \left(\frac{\chi_{\epsilon_i}}{\kappa_\epsilon^{2/3}} \right)^6 \tag{B23}$$

equations (B18) and (B19) can be simplified further to

$$Z(ZZ')' - \sqrt{ZZ'} = 1 \tag{B24}$$

The equation in this form can be solved parametrically as follows:

Let

$$\varphi = Z^2/2 \quad \text{and} \quad \lambda = d\varphi/d\zeta \tag{25a}$$

20

Equation (B24) becomes

$$\sqrt{2\varphi}\ \lambda\ \frac{d\lambda}{d\varphi} - \sqrt{\lambda} = 1 \tag{B25b}$$

which can be integrated to give

$$\varphi = 2\left[\sqrt{\lambda} - \frac{\lambda}{2} + \frac{\lambda^{3/2}}{3} - \ln(1 + \sqrt{\lambda})\right]^2 \tag{B26}$$

The solution of equation (B24) can finally be brought to the parametric form

$$Z = 2\left[\sqrt{\lambda} - \frac{\lambda}{2} + \frac{\lambda^{3/2}}{3} - \ln(1 + \sqrt{\lambda})\right] \tag{B27}$$

$$\zeta = \frac{1}{3}(1 + \sqrt{\lambda})^4 - \frac{22}{9}(1 + \sqrt{\lambda})^3 + 9(1 + \sqrt{\lambda})^2$$

$$- \frac{46}{3}(1 + \sqrt{\lambda}) + \frac{10}{3}\ln(1 + \sqrt{\lambda}) - 4\sqrt{\lambda}\ \ln(1 + \sqrt{\lambda})$$

$$+ 2\left[\ln(1 + \sqrt{\lambda})\right]^2 + \frac{76}{9} \tag{B28}$$

The pressure on the plate can now be found from the Newtonian-plus centrifugal formula as follows:

$$p = \gamma M_\infty^2 p_\infty \frac{d}{d\lambda}\left(Y_e\ \frac{dY_e}{d\lambda}\ \frac{d\lambda}{dx}\right) \tag{B29}$$

If equations (B27) and (B28) are differentiated and substituted into equation (B29) the pressures can be put into the form

$$\frac{p}{p_\infty}\ \frac{1}{4\gamma_\infty}\left(\frac{\kappa_\epsilon}{\chi_{\epsilon_i}^2}\right)^2 = \left(\frac{Z'}{\zeta'}\right)^2 \pm \frac{ZZ''}{(\zeta')^2} - \frac{ZZ'\zeta''}{(\zeta')^3} \equiv G(\lambda) \tag{B30}$$

The primes denote differentiation with respect to λ.

Having the solution to the pressure, the heat-transfer distribution can be found by substituting P/P_∞ from equation (B30) into the previously derived heat-transfer equation (B15). The heat-transfer equation is

$$-St \frac{PrM_{\infty}}{2s'(0)\sqrt{\gamma_{\infty}}} \left[\alpha_1 + \frac{\gamma_{\infty}-1}{2} M_{\infty}^2 I_1 r(\infty) + \left(\frac{T_W}{T_{\infty}} - \frac{T_{aw}}{T_{\infty}} \right) I_1 s(\infty) \right] \left(\frac{\kappa_\epsilon}{\chi_{\epsilon_i}^2} \right)^3$$

$$= \frac{G(\lambda)}{\sqrt{\int_0^\lambda G(\lambda) \zeta' \, d\lambda}}$$

(B31)

REFERENCES

1. Libby, Paul A.; and Cresci, Robert J.: Experimental Investigation of the Downstream Influence of Stagnation-Point Mass Transfer. J. Aero. Sci., vol. 28, no. 1, Jan. 1961, pp. 51-64.

2. Cresci, Robert J.; and Libby, Paul A.: The Downstream Influence of Mass Transfer at the Nose of a Slender Cone. J. Aero. Sci., vol. 29, no. 7, July 1962, pp. 815-826.

3. Rubesin, Morris W.; and Inouye, Mamoru: A Theoretical Study of the Effect of Upstream Transpiration Cooling on the Heat-Transfer and Skin-Friction Characteristics of a Compressible, Laminar Boundary Layer. NACA TN 3969, 1957.

4. Cresci, Robert J.: Theoretical Analysis of the Downstream Influence of Stagnation Point Mass Transfer. WADD Tech. Rep. 60-434, Nov. 1961.

5. McMahon, Howard M.: An Experimental Study of the Effect of Mass Injection at the Stagnation Point of a Blunt Body. Calif. Inst. of Tech., GALCIT Memo. 42, May 1, 1958.

6. Baum, Eric: Effect of Boundary Layer Blowing on the Laminar Separated Shear Layer. Electro-Optical Systems Inc., EOS-RN-9, Apr. 1963.

7. Baum, E.; King, H. H.; and Denison, M. R.: Recent Studies of the Laminar Base Flow Region. AIAA Preprint 64-5, 1964.

8. King, Hartley H.: An Analysis of Base Heat Transfer in Laminar Flow. Electro-Optical Systems Inc., EOS-RN-14, Sept. 1963.

9. King, Hartley H.; and Baum, Eric: Enthalpy and Atom Profiles in the Laminar Separated Shear Layer. Electro-Optical Systems Inc., EOS-RN-8, March 1963.

10. Howe, John T.: Some Finite Difference Solutions of the Laminar Compressible Boundary Layer Showing the Effects of Upstream Transpiration Cooling. NASA MEMO 2-26-59A, 1959.

11. Gowen, Forrest E.; and Hopkins, Vaughn D.: A Wind Tunnel Using Arc-Heated Air for Mach Numbers From 10 to 20. Second National Symposium on Hypervelocity Techniques, Denver, Colorado, March 19-20, 1962. Advances in Hypervelocity Techniques, Arthur M. Krill, ed., N. Y., Plenum, 1962, pp. 27-46.

12. Dimeff, John; Lane, James W.; and Coon, Grant W.: New Wide-Range Pressure Transducer. Rev. Sci. Instr., vol. 33, no. 8, Aug. 1962, pp. 804-811.

13. Matting, Fred W.; and Chapman, Dean R.: Generalized Ablation Analysis With Application to Heat-Shield Materials and Tektite Glass. AIAA Paper 65-490, 1965.

14. Vojvodich, Nick S.: The Performance of Ablative Materials in a High-Energy, Partially Dissociated, Frozen Nitrogen Stream. NASA TN D-1205, 1962.

15. Yee, Layton: Free-Flight Measurements of Heat Transferred to the Apollo Afterbody With and Without Heat Shield Ablation. NASA TM X-1096, 1965.

16. Chapman, Dean R.: A Theoretical Analysis of Heat Transfer in Regions of Separated Flow. NACA TN 3792, 1956.

17. Faulders, C. R.: Heat Transfer in the Laminar Boundary Layer With Ablation of Vapor of Arbitrary Molecular Weight. J. Aero. Sci., vol. 29, no. 1, Jan. 1962, pp. 76-86.

18. Cheng, Hsien K.: Hypersonic Flow With Combined Leading-Edge Bluntness and Boundary-Layer Displacement Effect. Cornell Aero. Lab. Rep. AF-1285-A-4, Aug. 1960.

19. Cheng, H. K.; Hall, J. Gordon; Golian, T. C.; and Hertzberg, A.: Boundary-Layer Displacement and Leading-Edge Bluntness Effects in High-Temperature Hypersonic Flow. J. Aero. Sci., vol. 28, no. 5, May 1961, pp. 353-381.

20. Lee, George; and Sundell, Robert E.: Heat-Transfer and Pressure Distributions on Apollo Models at $M = 13.8$ in an Arc-Heated Wind Tunnel. NASA TM X-1069, 1965.

21. Lees, Lester: Laminar Heat Transfer Over Blunt-Nosed Bodies at Hypersonic Flight Speeds. Jet Propulsion, vol. 26, no. 4, Apr. 1956, pp. 259-269.

22. Low, George M.: The Compressible Laminar Boundary Layer With Fluid Injection. NACA TN 3404, 1955.

23. Emmons, Howard W.; and Leigh, D. C.: Tabulation of the Blasius Function With Blowing and Suction. British Aero. Res. Council, ARC Tech. Rep. C. P. 157, 1954.

24. Chapman, Dean R.; and Rubesin, Morris W.: Temperature and Velocity Profiles in the Compressible Laminar Boundary Layer With Arbitrary Distribution of Surface Temperature. J. Aero. Sci., vol. 16, no. 9, Sept. 1949, pp. 547-565.

TABLE I.- NOMINAL TEST CONDITIONS

Test condition	M	h_t J/kg$\times 10^{-6}$	p_t N/m$^2\times 10^{-6}$	$Re_D\times 10^{-3}$
1	8.3	1.628	1.0	22.00
2	8.1	2.324	1.0	7.10
3	7.8	3.486	.75	2.80
4	7.4	4.648	.50	.65
5	6.8	5.815	.37	.60
6	6.2	6.972	.25	.30
7	5.8	9.296	.25	.20

9

8

M_∞

7

6

5

	$p_t \times 10^{-6}$	$h_t \times 10^{-6}$
○	0.75	3.486
□	.37	6.390
◇	.25	9.296

.04   .02   0   .02   .04   .06   .08   .10   .12

Radial distance from centerline, m
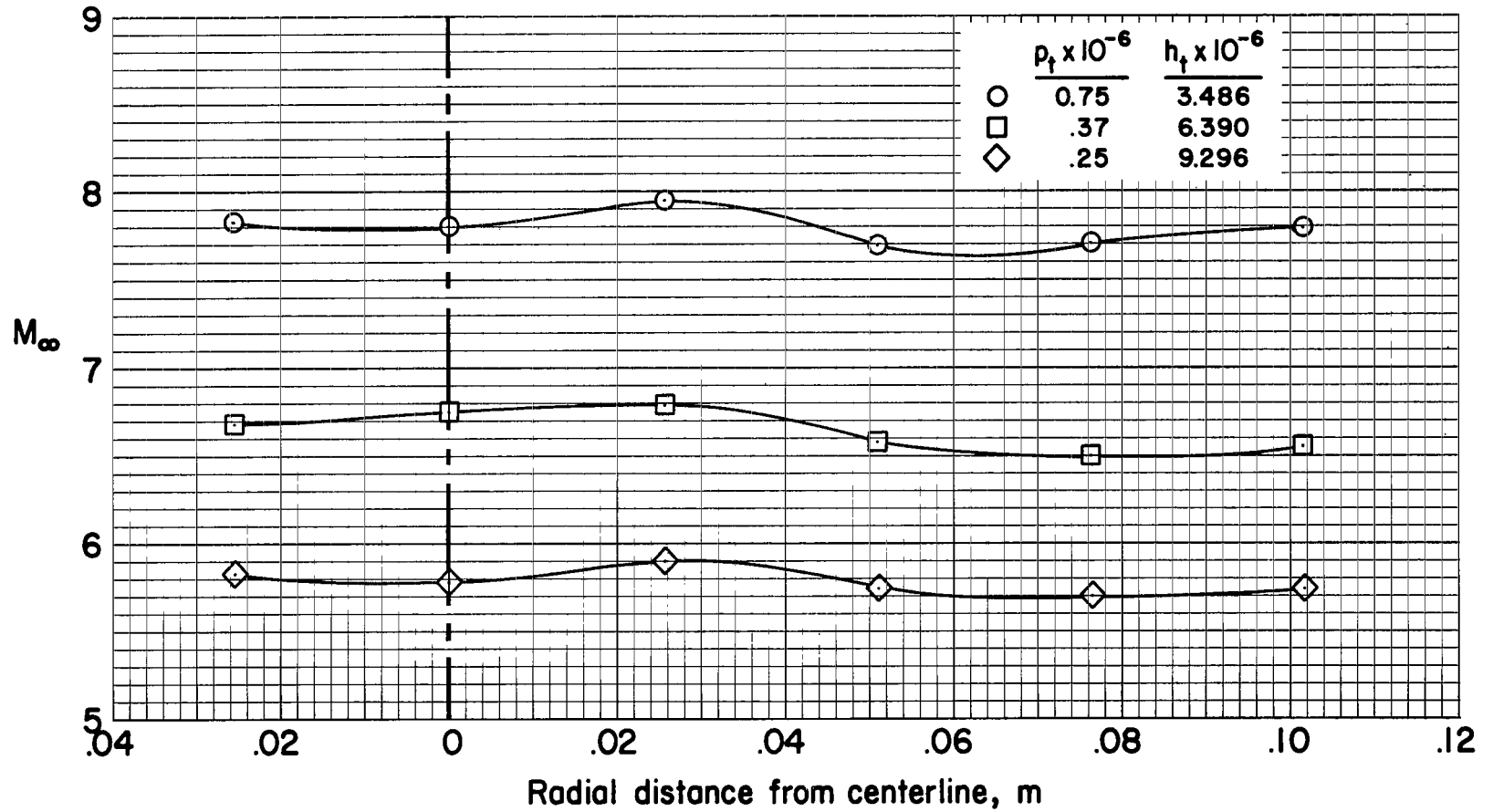
Figure 1.- Typical Mach number distribution in test section.
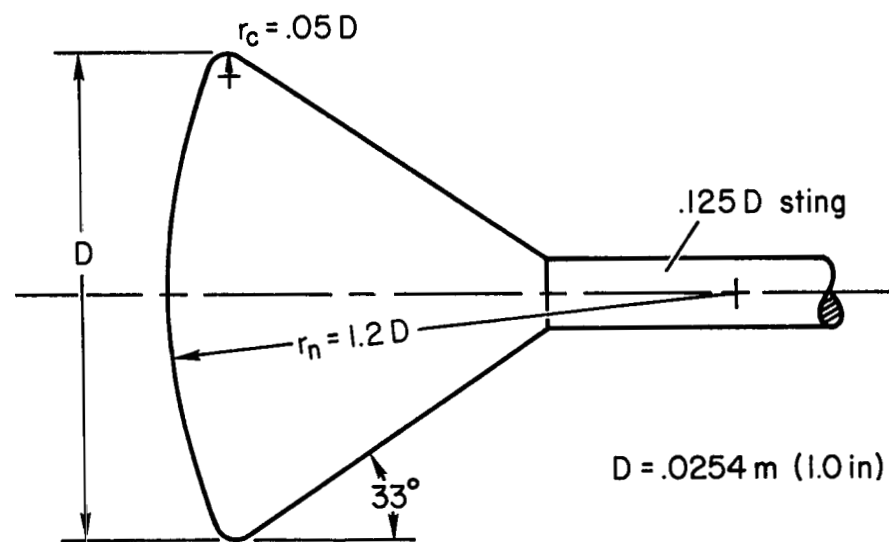
Figure 2.- Sketch of model.
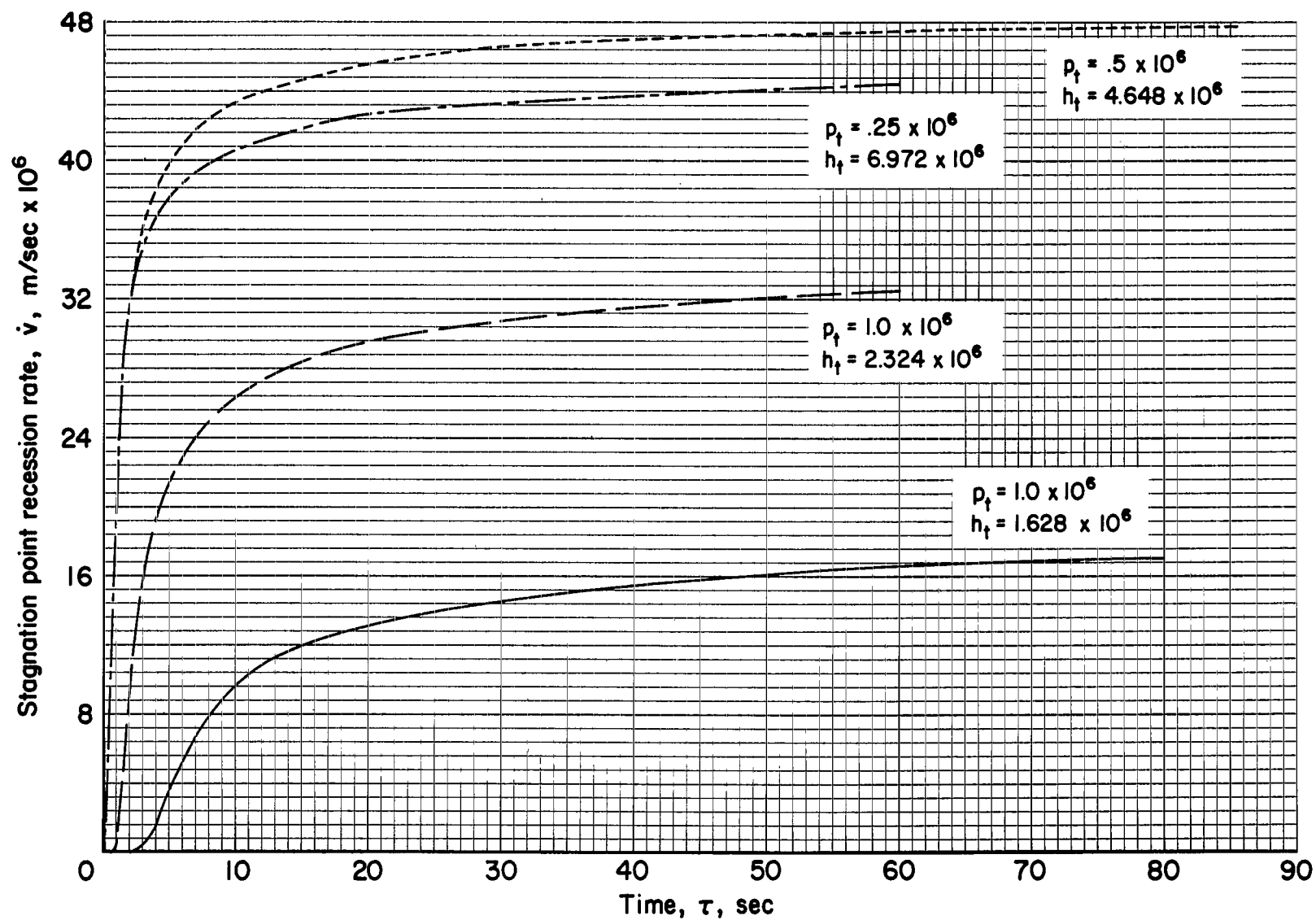
. . Figure 3.- Time history of calculated stagnation-point recession rates at four typical test conditions.
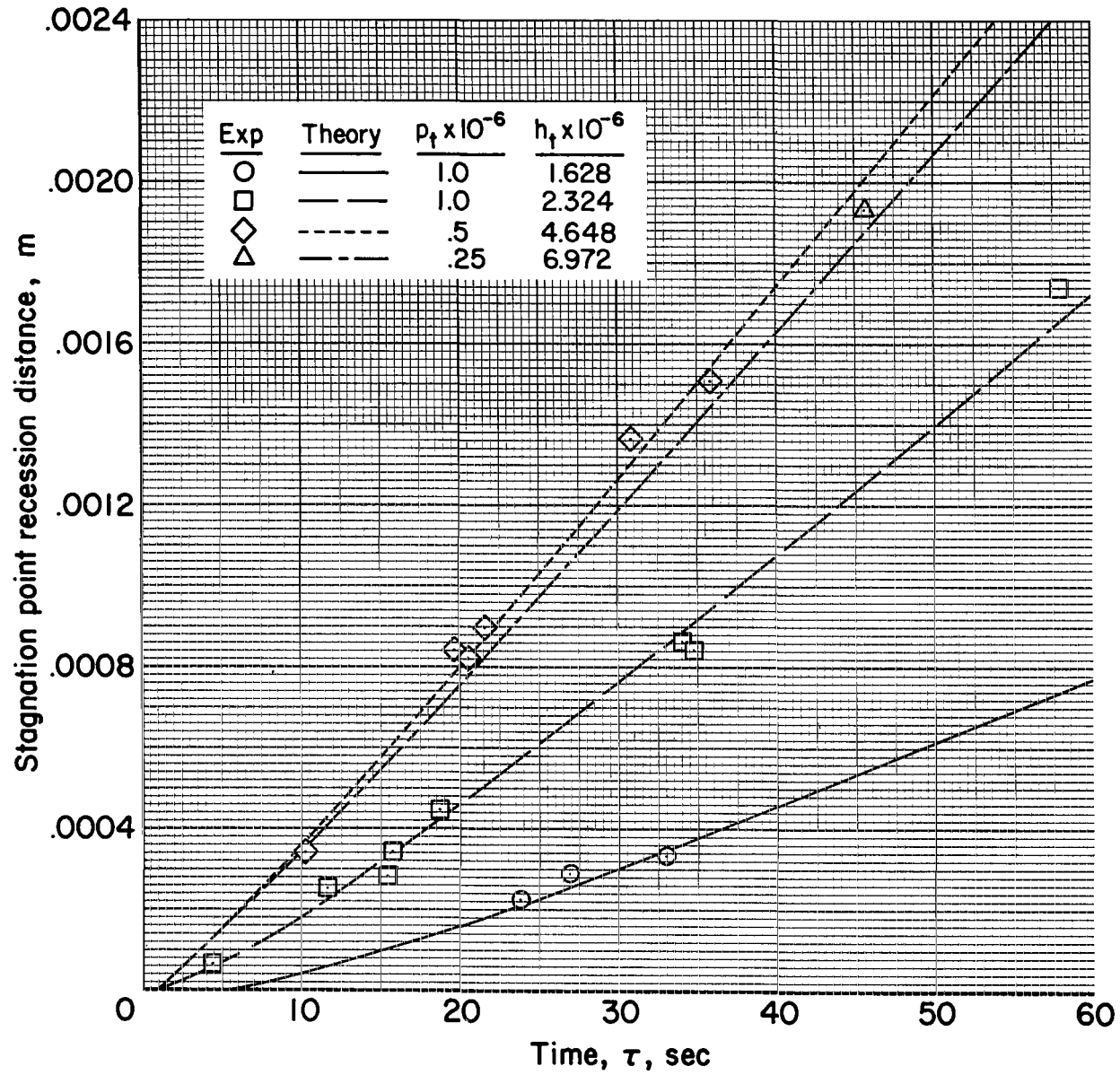
Figure 4.- Comparison of experimental and theoretical stagnation-point recession distance.
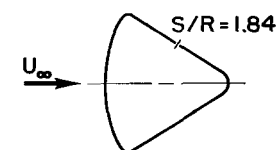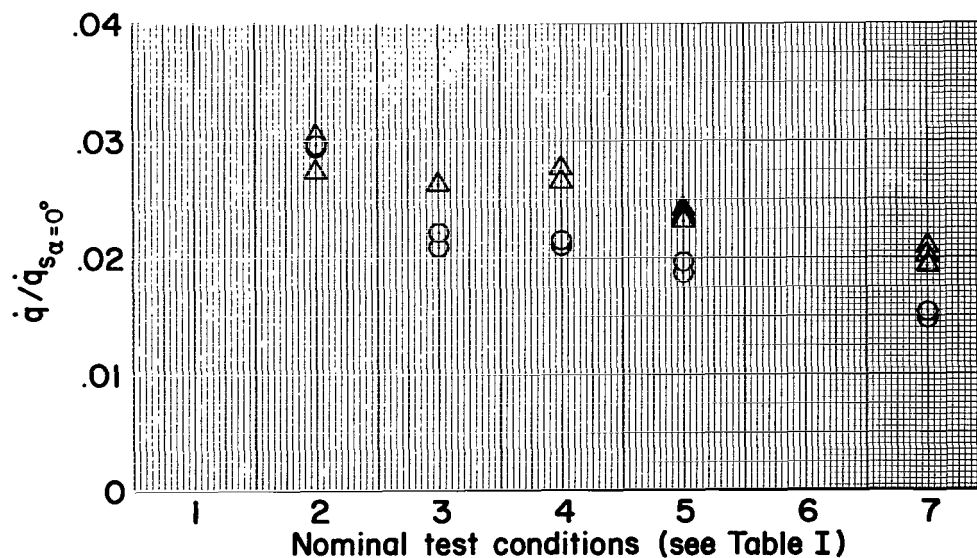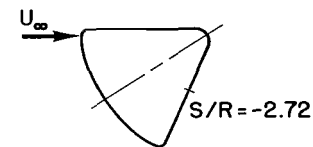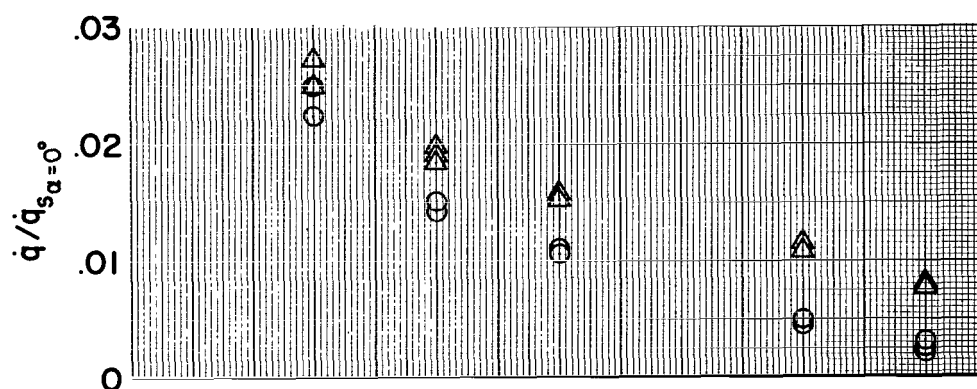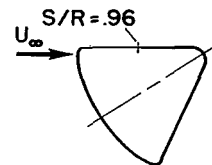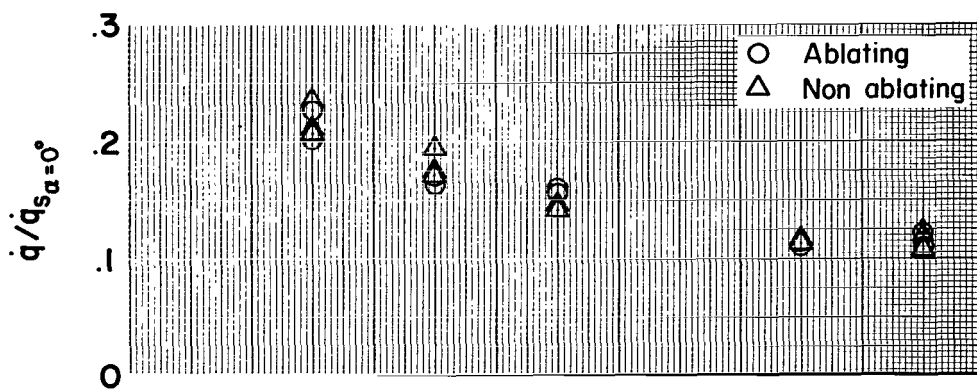
Figure 5.- Comparisons of afterbody heating rates with and without
injection at seven test conditions.
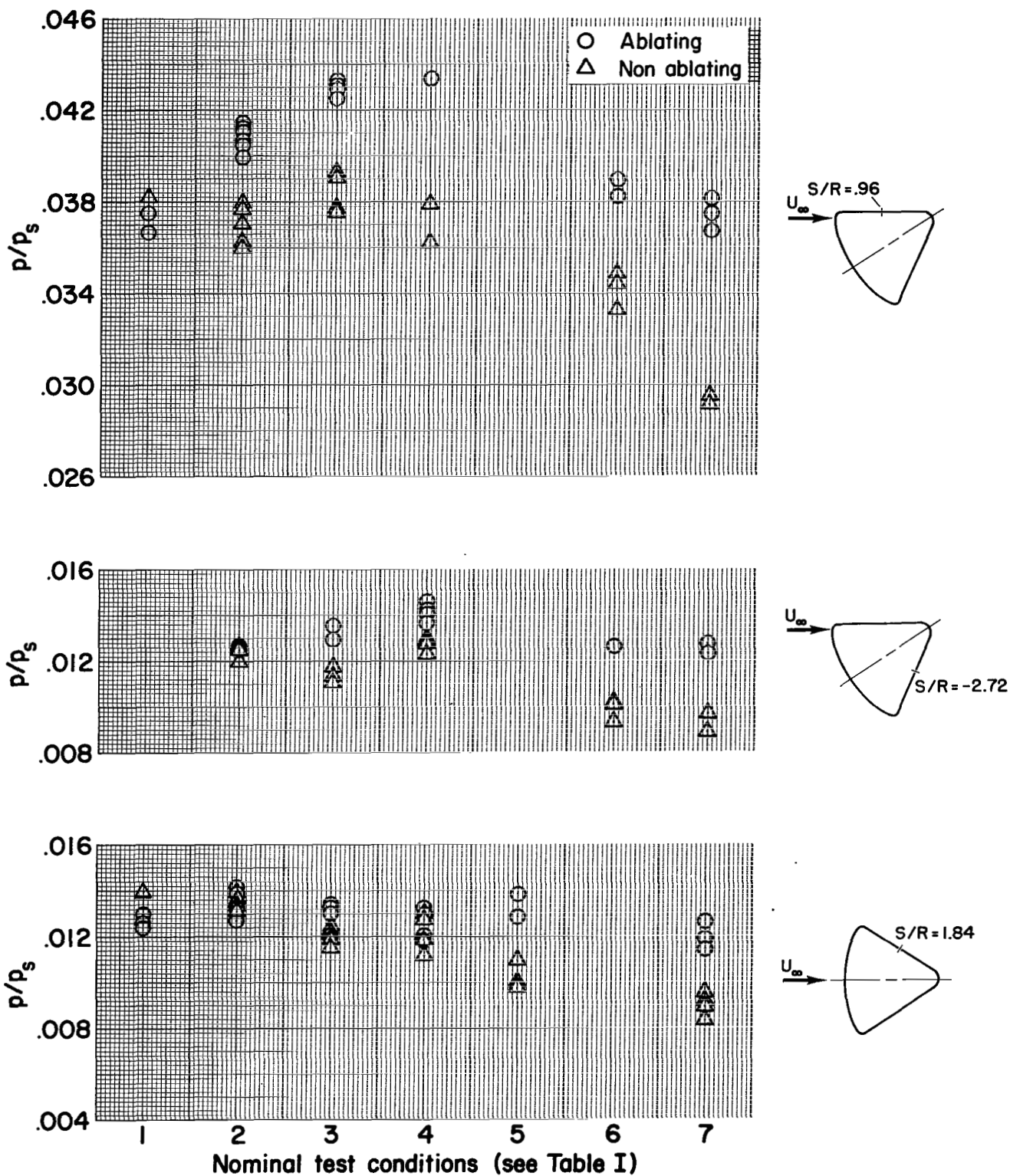
Figure 6.- Comparisons of afterbody pressures with and without injection at seven test conditions.

$\alpha = 33^{\text{O}}$

$\alpha = 0^{\text{O}}$
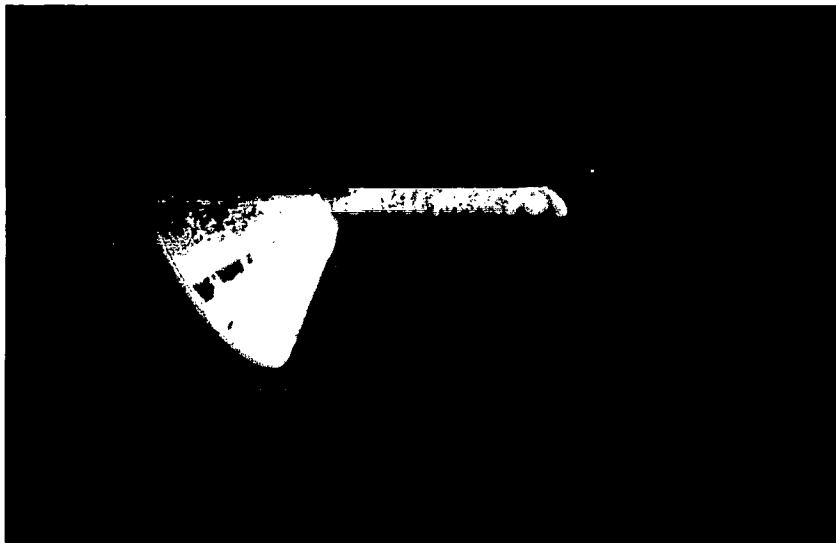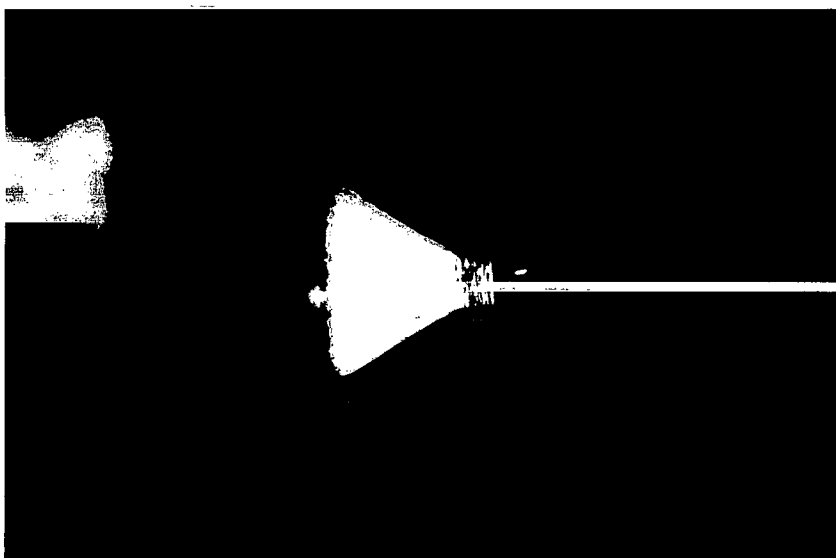
Figure 7.- Oil film pattern on Apollo afterbody.
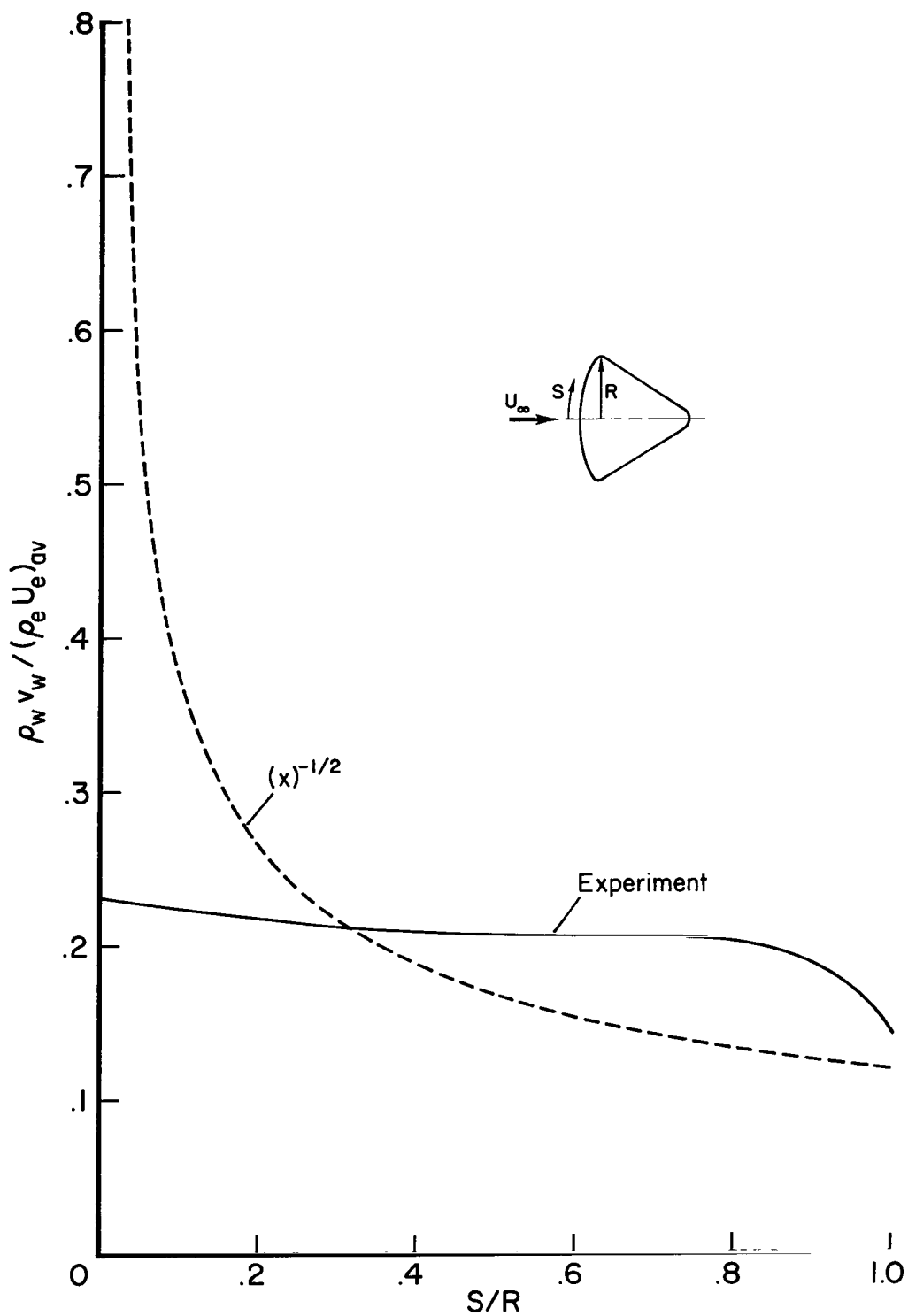
(a) $\alpha = 0$

Figure 8.- Comparison of theoreoretical and experimental mass injected distributions.

(b) Leeward side, $\alpha = 33^\circ$.

Figure 8.- Concluded.
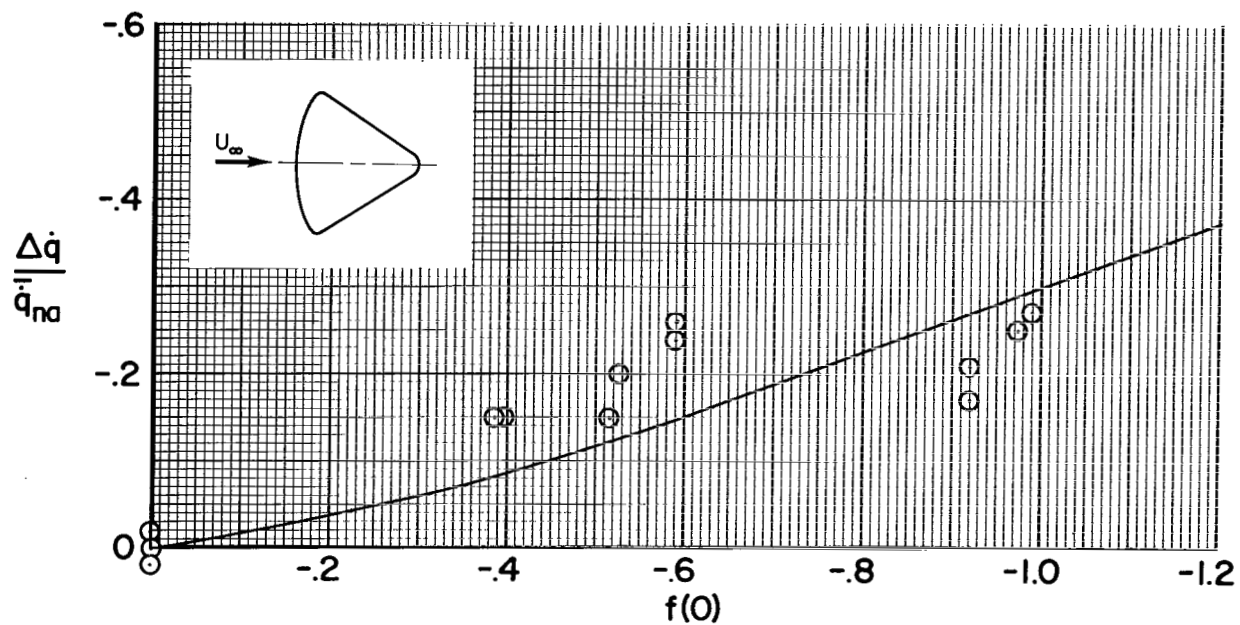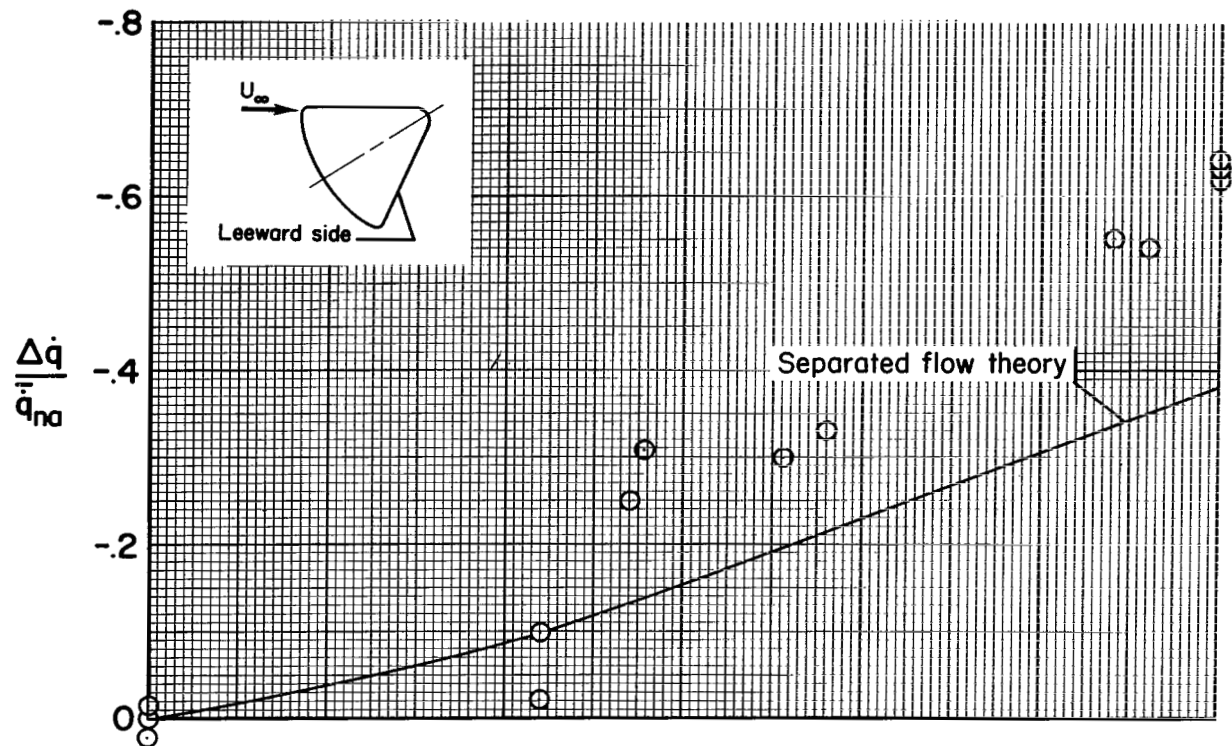
(a) Heat transfer.

Figure 9.- Correlation of data and comparison with theory for $\alpha = 0^{\circ}$ and $\alpha = 33^{\circ}$ leeward side.
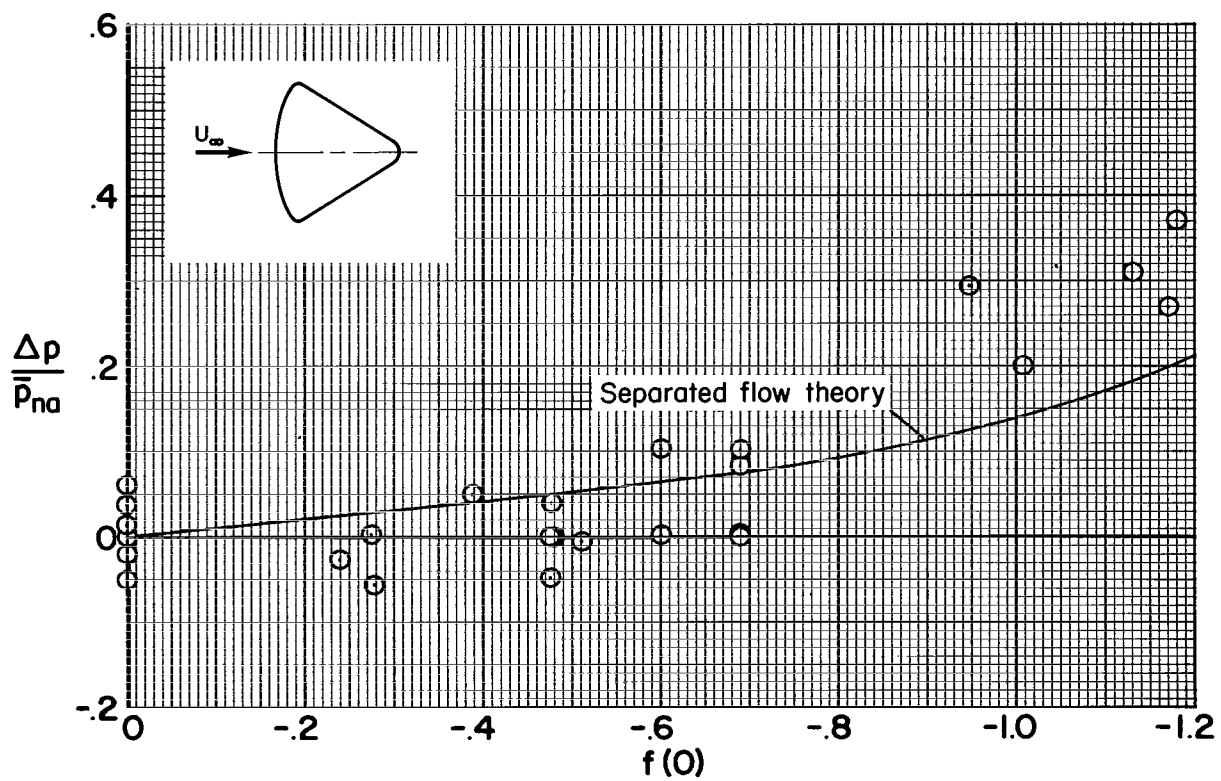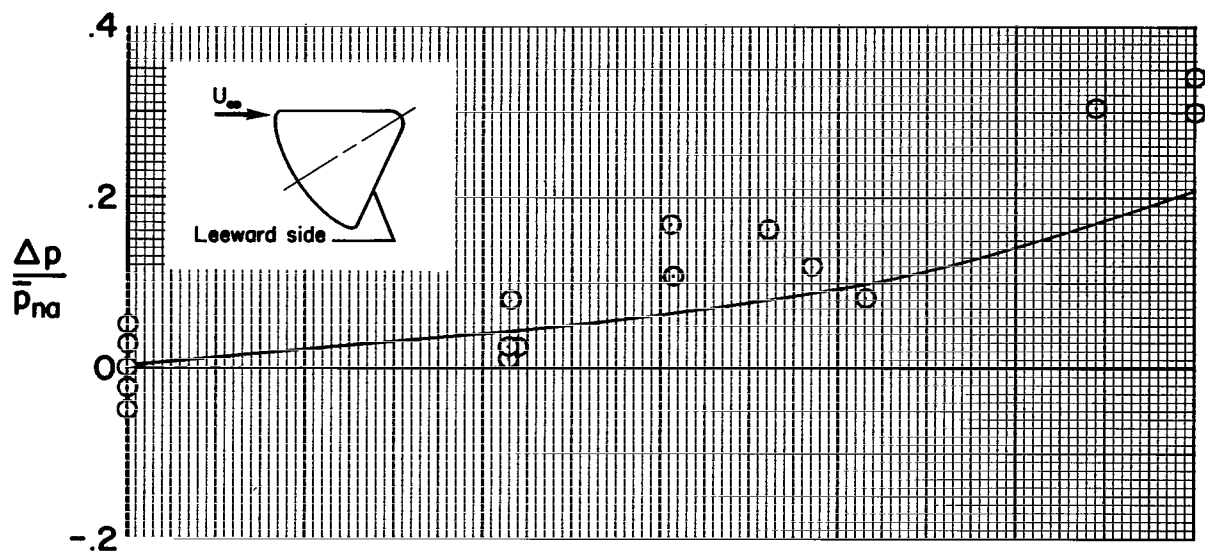
(b) Pressures.

Figure 9.- Concluded.
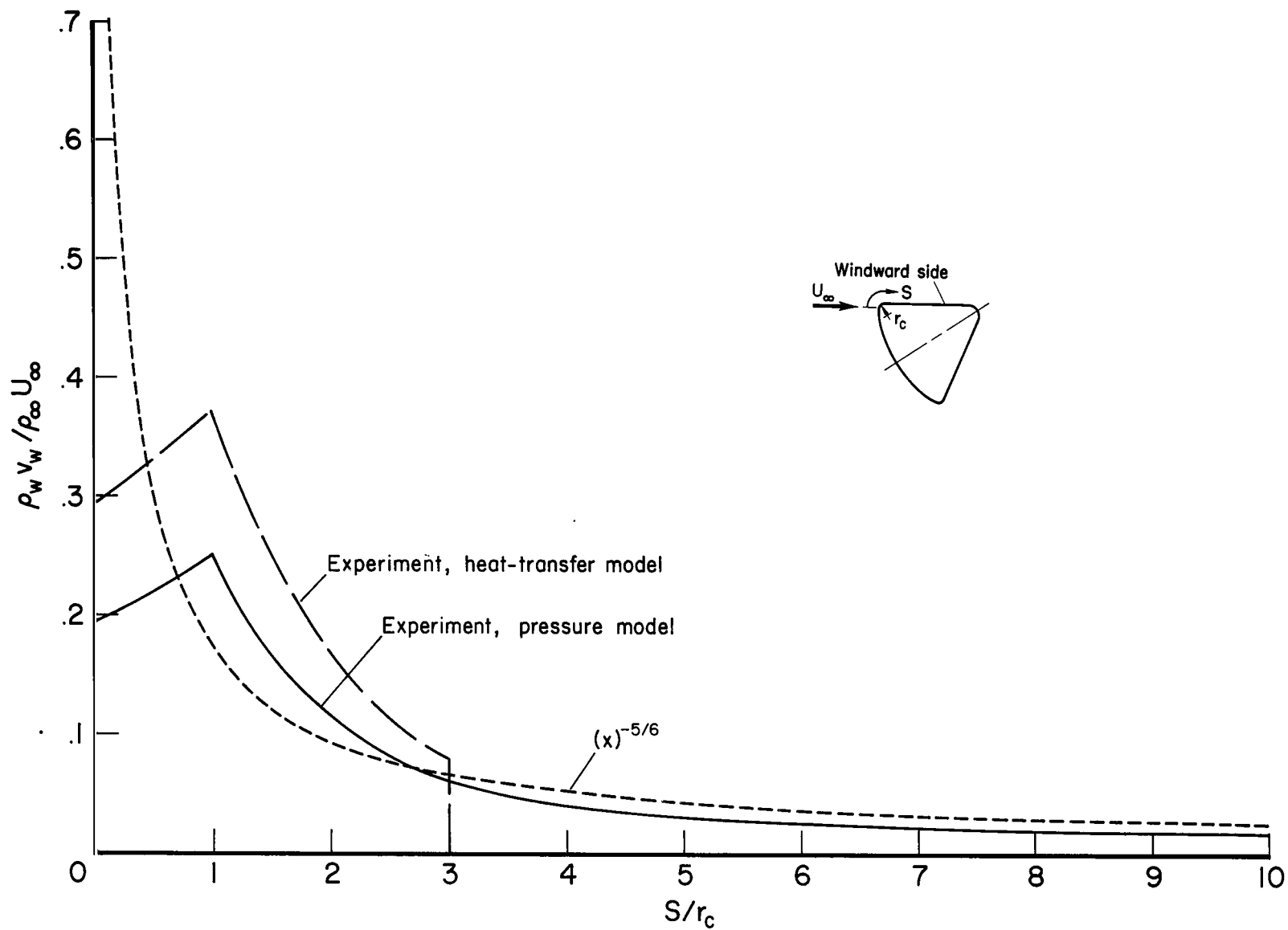
Figure 10.- Comparison of theoretical and experimental mass injected distributions; windward side, $\alpha = 33^\circ$.
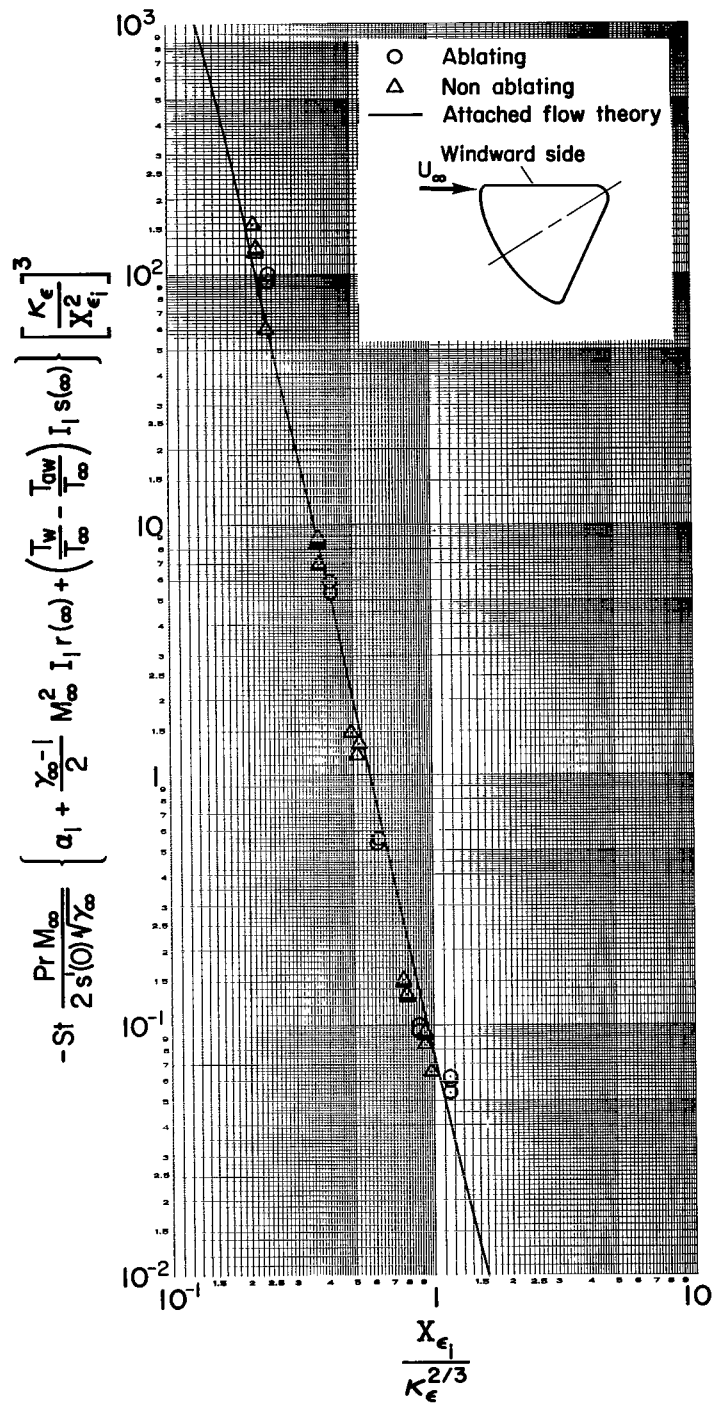
(a) Heat transfer.

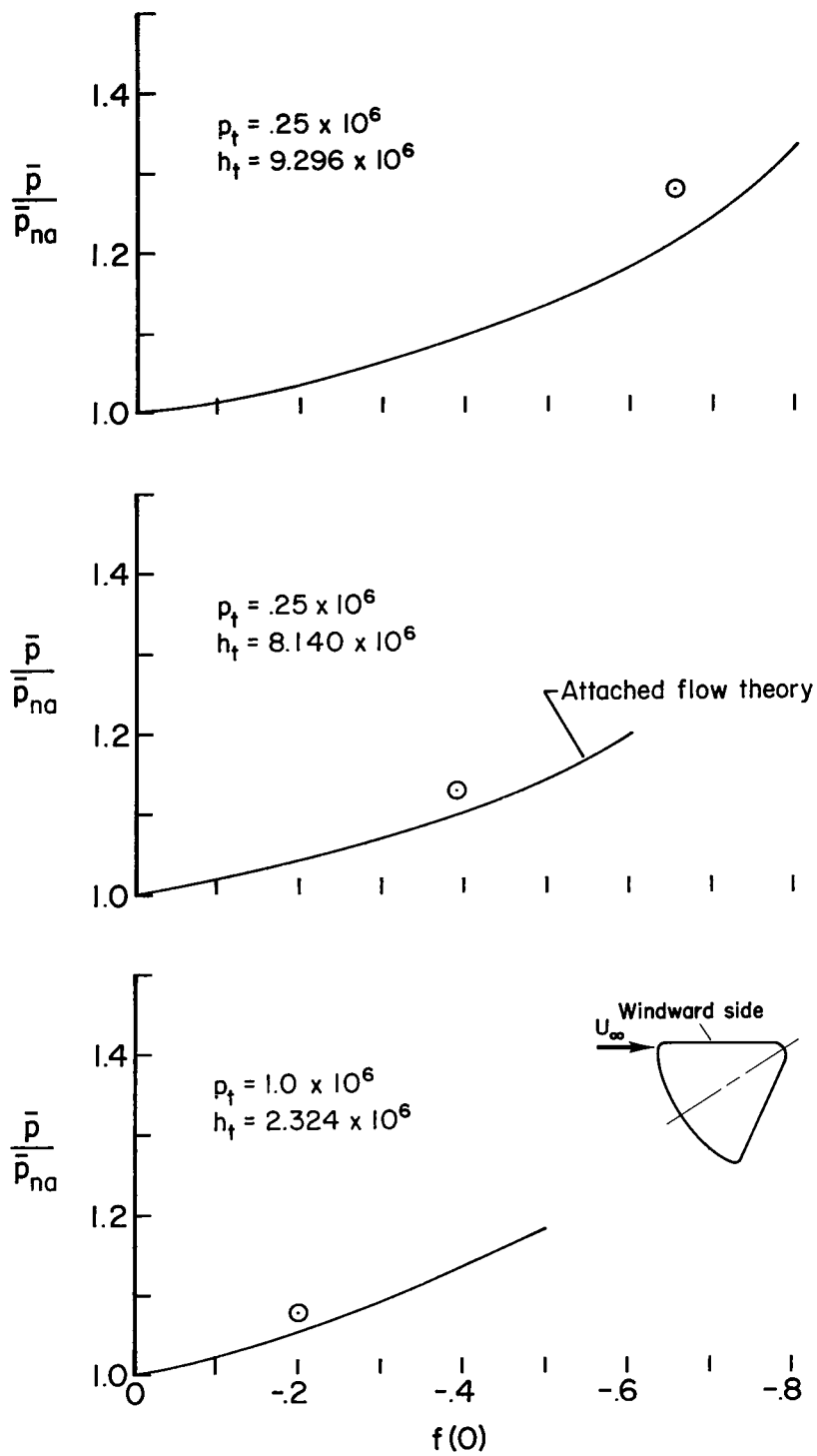Figure 11.- Correlation of data on the windward side at $\alpha = 33^\circ$ and comparison with theory.
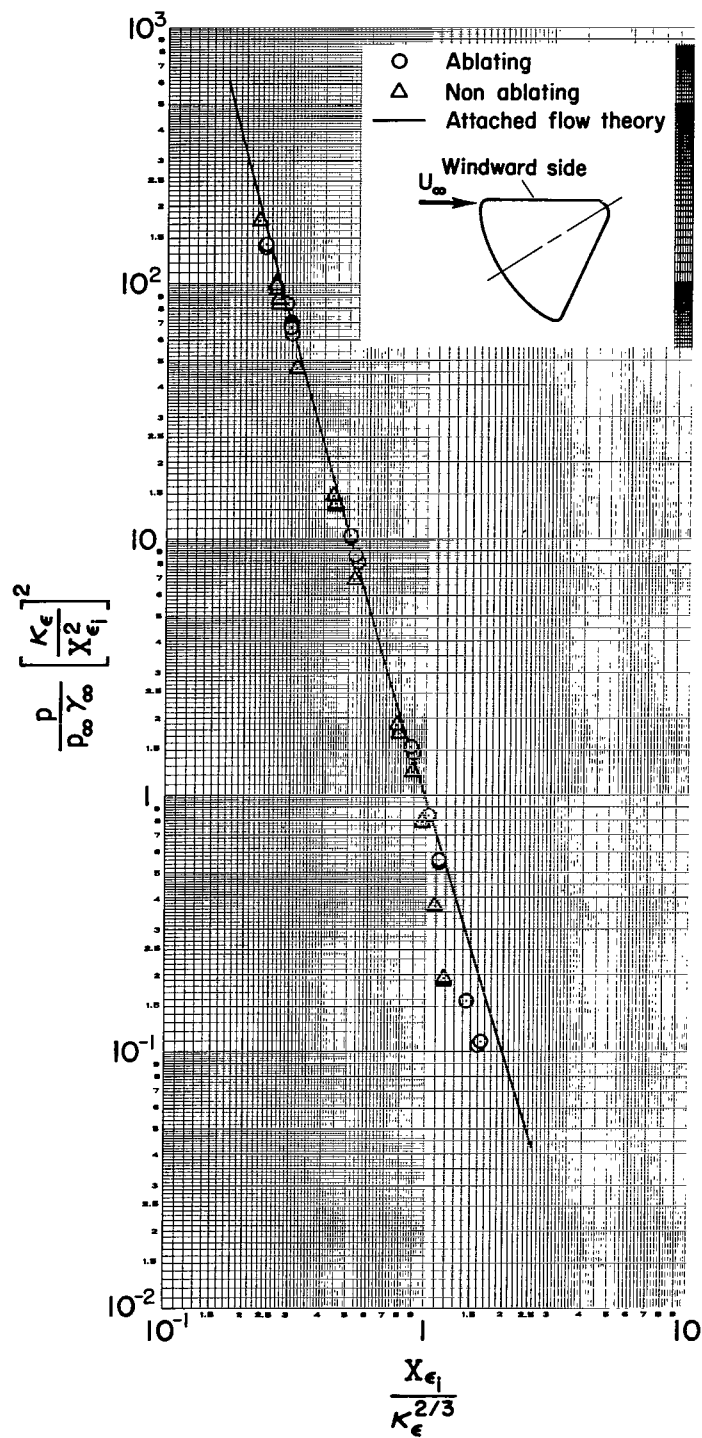
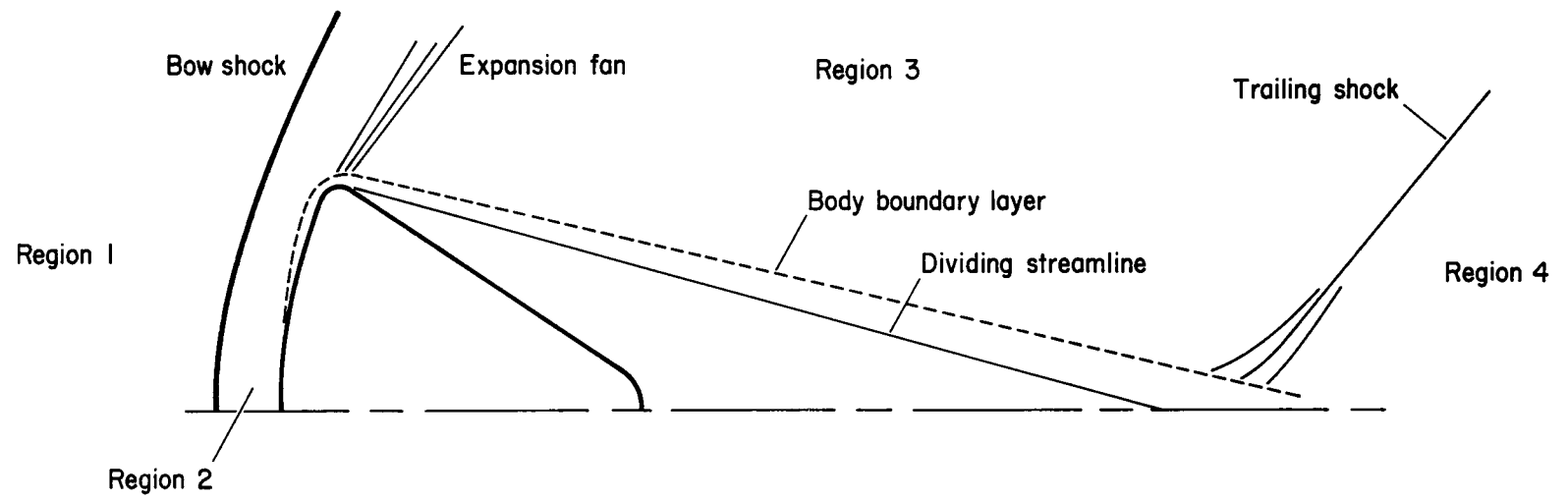(b) Afterbody pressures.

Figure 11.- Concluded.
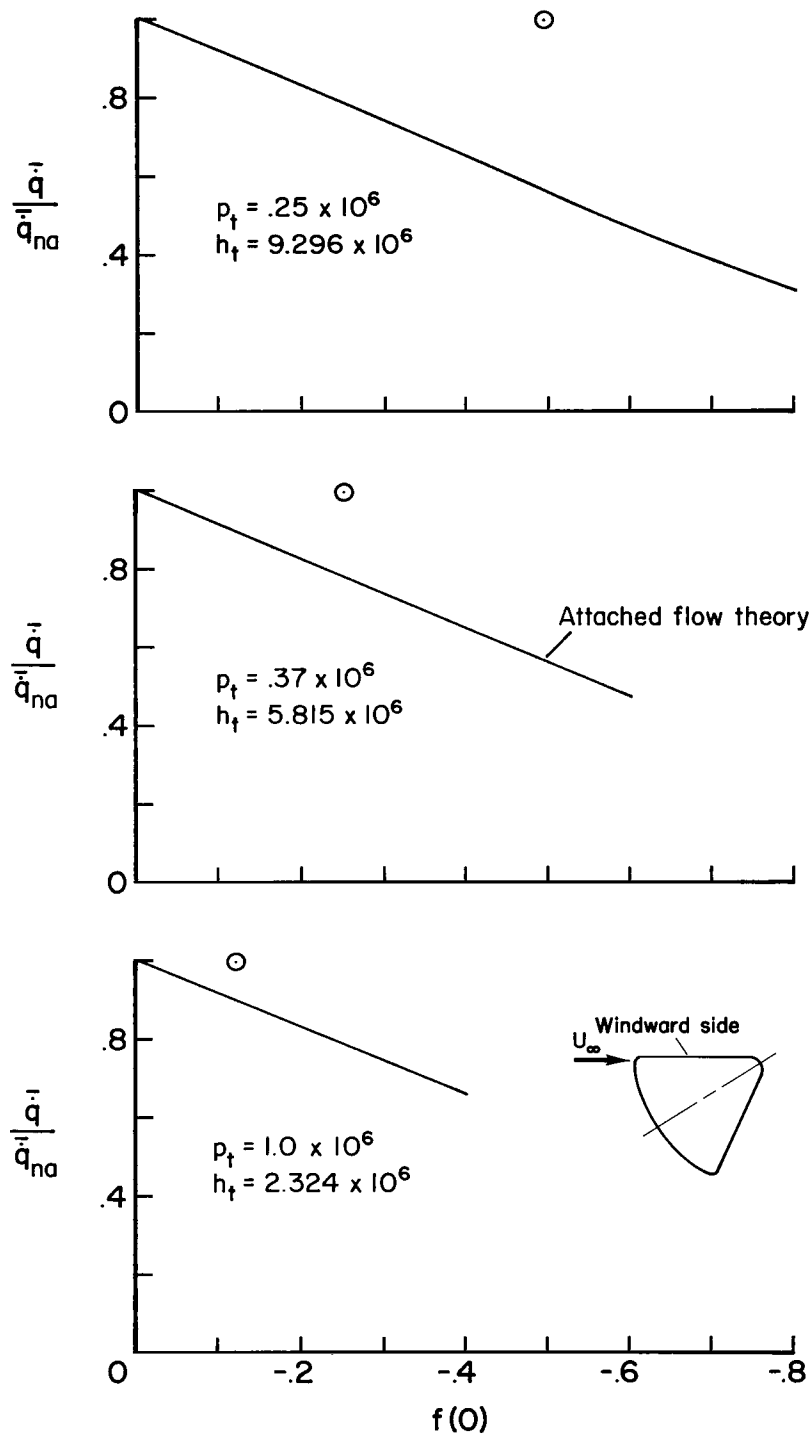
(a) Heat transfer.

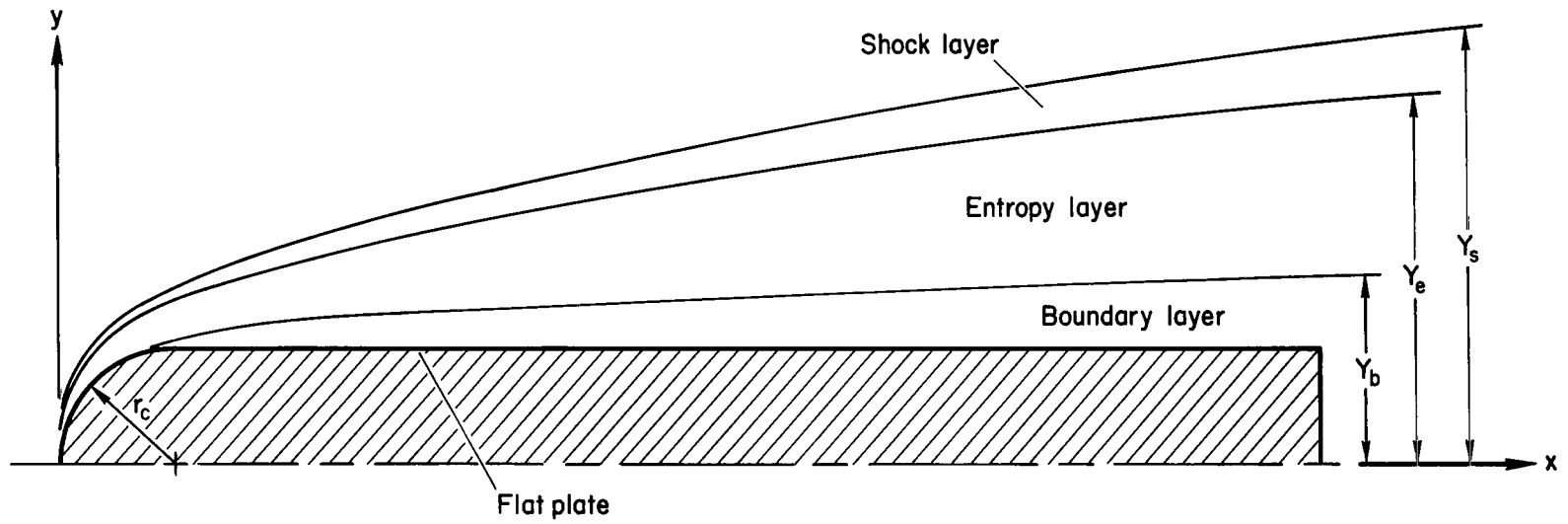Figure 12.- Effect of mass injection on heat transfer and pressures at $\alpha = 33^o$; windward side.

$p_t = .25 \times 10^6$
$h_t = 9.296 \times 10^6$

$p_t = .25 \times 10^6$
$h_t = 8.140 \times 10^6$

Attached flow theory

$p_t = 1.0 \times 10^6$
$h_t = 2.324 \times 10^6$

U_∞ Windward side

(b) Pressures.

Figure 12.- Concluded.

(a) Separated flow.

Figure 13.- Assumed flow models.

(b) Attached flow.

Figure 13.- Concluded.

NASA SCIENTIFIC AND TECHNICAL PUBLICATIONS

TECHNICAL REPORTS: Scientific and technical information considered important, complete, and a lasting contribution to existing knowledge.

TECHNICAL NOTES: Information less broad in scope but nevertheless of importance as a contribution to existing knowledge.

TECHNICAL MEMORANDUMS: Information receiving limited distribution because of preliminary data, security classification, or other reasons.

CONTRACTOR REPORTS: Technical information generated in connection with a NASA contract or grant and released under NASA auspices.

TECHNICAL TRANSLATIONS: Information published in a foreign language considered to merit NASA distribution in English.

TECHNICAL REPRINTS: Information derived from NASA activities and initially published in the form of journal articles.

SPECIAL PUBLICATIONS: Information derived from or of value to NASA activities but not necessarily reporting the results of individual NASA-programmed scientific efforts. Publications include conference proceedings, monographs, data compilations, handbooks, sourcebooks, and special bibliographies.

Details on the availability of these publications may be obtained from:

SCIENTIFIC AND TECHNICAL INFORMATION DIVISION

NATIONAL AERONAUTICS AND SPACE ADMINISTRATION

Washington, D.C. 20546